

AN ABSTRACT OF THE THESIS OF

Ari A. R. Foley for the degree of Master of Science in Nuclear Engineering presented on May 30, 2019.

Title: Short-lived Photofission Product Yields and Analytical Methods for Nuclear Forensic Application

Abstract approved: _____
Haori Yang

The evaluated nuclear data widely used in computational tools suffer from inaccuracies and large relative uncertainties, particularly with respect to short-lived and low-yield fission products. The existing data are often based on nuclear models, and limited experimental measurements of these fission product yields have been performed. This work seeks to validate and improve, where applicable, the current fission product yield data in the ENDF library using experimental measurements, particularly for the photofission of ^{238}U and ^{232}Th .

Much of the measurable fission products would have decayed away in experiments that require sample transfer from the linear accelerator to an auxiliary detection setup, resulting in low count rates and large uncertainty in the calculated yield of fission products for those that are short-lived ($T_{1/2} \leq 50$ s). A high-purity germanium detector and a pneumatic transfer system were employed for measurements of short-lived fission products, collecting data between accelerator irradiation and counting cycles. These experiments resulted in measured cumulative fission product yields for ^{238}U and ^{232}Th at bremsstrahlung X-ray endpoint energies of 8, 14, and 20 MeV. These are reported with their excitation energies to allow for reliable comparison among other experimental data sets.

©Copyright by Ari A. R. Foley

May 30, 2019

All Rights Reserved

Short-lived Photofission Product Yields and Analytical Methods for Nuclear
Forensic Application

by

Ari A. R. Foley

A THESIS

submitted to

Oregon State University

in partial fulfillment of
the requirements for the
degree of

Master of Science

Presented May 30, 2019
Commencement June 2019

Master of Science thesis of Ari A. R. Foley presented on May 30, 2019.

APPROVED:

Major Professor, representing Nuclear Engineering

Head of the School of Nuclear Science and Engineering

Dean of the Graduate School

I understand that my thesis will become part of the permanent collection of Oregon State University libraries. My signature below authorizes release of my thesis to any reader upon request.

Ari A. R. Foley, Author

ACKNOWLEDGEMENTS

Dr. Haori Yang, for the longtime support and encouragement as my advisor.

Dr. Matt Kinlaw, for being my mentor in both photonuclear physics and fly fishing.

Dr. Camille Palmer, Dr. Steve Reese, and Dr. Kenneth Krane, for acting as my graduate committee, especially around difficult schedules.

Dr. Mathew Snow and Ms. Jessica Ward at Idaho National Laboratory, for performing the ICP-MS analysis on the uranium and thorium foils.

Dr. Alan Hunt, Chad O'Neill, Kevin Folkman, and Brian Berls at the Idaho Accelerator Center, for helping to operate and perform the week of experiments.

Alex Dueñas, for acting as my replacement abuelita.

This research made use of the resources of the High Performance Computing Center at Idaho National Laboratory, which is supported by the Office of Nuclear Energy of the U.S. Department of Energy and the Nuclear Science User Facilities under Contract No. DE-AC07-05ID14517.

TABLE OF CONTENTS

	<u>Page</u>
1 Introduction	1
1.1 Motivation	2
1.2 Objectives	3
1.3 Document Overview	4
2 Background and Theory	6
2.1 The Photofission Process	6
2.1.1 The Giant Dipole Resonance	8
2.1.2 Multimode-Fission Model	9
2.2 Fission Products	13
2.3 High-Energy Photon Sources	15
2.3.1 Yield from Bremsstrahlung Source	15
2.3.2 Excitation Energy from Bremsstrahlung X-Rays	16
2.4 Interaction of Photons with Matter	17
2.4.1 Photoelectric Effect	18
2.4.2 Compton Scattering	19
2.4.3 Pair Production	20
2.4.4 Photonuclear Absorption	20
2.5 High-Purity Germanium Detectors	21
2.6 High-Rate Applications	22
2.7 Nuclear Forensics Applications	24
3 Materials and Methods	25
3.1 Introduction	25
3.2 Description of Targets	25
3.2.1 Target Geometry	26
3.2.2 Target Composition	27
3.3 In-Hall Experimental Setup	30

TABLE OF CONTENTS (Continued)

	<u>Page</u>
3.3.1 25 MeV Linear Accelerator	31
3.3.2 Pneumatic Transfer System	33
3.3.3 Ortec Gamma-X HPGe	35
3.3.4 Model for Detector Energy Efficiency	37
3.3.5 List-mode data collection	43
3.4 Fission Product Yield Analysis	44
3.4.1 Fission Product Yield Using Single Timing Bin	44
3.4.2 Fission Product Yield Using an Integral Solver	46
3.5 Calculation of Photofission Events From ^{237}U Production	48
4 Characterization and Simulation	52
4.1 Introduction	52
4.2 Bremsstrahlung X-ray Flux on Target	52
4.2.1 Calculation of Photofission Yield Per Pulse Using Simulation	54
4.2.2 YZ Mesh Tally of Photon Beam on Target	55
4.2.3 3D Mesh Tally of Bremsstrahlung X-Ray Production	57
4.3 Uncertainty Considerations on the Photofission Yield Per Pulse .	59
4.3.1 Target Offset from Beam	59
4.3.2 Neutron Fission in Target	61
4.3.3 Fission of Impurity Actinides	62
4.4 Fission Events Per Linac Pulse	64
4.5 Modeling of HPGe Detector Response in MCNP6	64
5 Results	70
5.1 Overview	70
5.2 Fission Product Yields for ^{238}U	74
5.3 Fission Product Yields for ^{232}Th	78
6 Conclusions	83
6.1 Future Work	84

LIST OF FIGURES

<u>Figure</u>		<u>Page</u>
1 Time scale and description of both absorption, fission, and finally the prompt and delayed emissions following photon-induced fission.	8	
2 Compilation of ENDF-B/VII.0 evaluated cross $\sigma(\gamma,f)$ for actinide targets.	10	
3 Fit of the SL, STI, and STII fission modes using five Gaussian peaks applied to ENDF-B/VII.0 fractional mass yield data for fast (left) and DT (right) neutron fission of ^{238}U (top) and ^{232}Th (bottom).	12	
4 Uranium sample cut and secured in sample bag with teflon tape (left), Th sample as attached on sample holder of the pneumatic track (right).	26	
5 Attenuation of ^{152}Eu γ -rays in 0.1445 ± 0.0007 mm thick uranium foil fit to determine ρx ($\frac{\text{g}}{\text{cm}^3}$).	28	
6 Attenuation of ^{152}Eu γ -rays in 0.0567 ± 0.0005 mm thick thorium foil fit to determine ρx ($\frac{\text{g}}{\text{cm}^3}$).	29	
7 Photograph of full in-hall experimental setup at the Idaho Accelerator Center (middle), view of detector end of the pneumatic track (left), linac end of the pneumatic track showing sample placement (right).	31	
8 Schematic of the 25 MeV Electron Linear Accelerator at the Idaho Accelerator Center.	32	
9 Simulated bremsstrahlung X-ray flux incident on target at 8, 14, and 20 MeV endpoint energies (right axis) with reference to ^{238}U and ^{232}Th (γ,f) cross sections (left axis).	34	
10 Diagram of sample geometry on pneumatic track at both the irradiation end (top) and the measurement end (bottom).	35	
11 Measured γ -ray spectra on ADC2 used in the efficiency calibration for each sources of the in-hall HPGe detector. Energy range in efficiency calibration is from lowest energy at 53.161 keV to highest energy at 1408.006 keV.	36	
12 Ortec Gamma-X Coaxial HPGe efficiency, models (in red) and measured (in black) for ADC 1	42	
13 Ortec Gamma-X Coaxial HPGe efficiency, models (in red) and measured (in black) for ADC 2.	43	
14 ^{238}U irradiated at $B=8$ MeV list-mode data parsed into 2 s interval bins to visualize the decay of ^{99}Zr by its 469 keV peak.	47	
15 $^{238}\text{U}(\gamma,n)$, $^{238}\text{U}(\gamma,f)$, and $^{232}\text{Th}(\gamma,f)$ cross sections used in calculating photofission events per pulse.	49	
16 Measured energy distribution of the $B=8$, 14, and 20 MeV electron beams.	54	
17 MCNP6 produced bremsstrahlung X-ray spectra incident on target with endpoint energies 8, 14, and 20 MeV.	56	
18 Transparent glass slides discolored by the electron beam at the sample position for endpoint energies $B=8$, 14, and 20 MeV.	57	

LIST OF FIGURES (Continued)

<u>Figure</u>	<u>Page</u>
19 MCNP6-produced intensity distributions of the bremsstrahlung X-ray beam (top) and electrons (bottom) at sample position at $B=8$, 14, and 20 MeV.	58
20 3D visualization of the electron and bremsstrahlung X-ray beams for 8, 14, and 20 MeV endpoint energies produced with MCNP6 simulation.	59
21 (Top) Ratio of $^{238}\text{U}(\gamma, f)$ and $^{232}\text{Th}(\gamma, f)$ yields with respect to offset from center to the left and down in thorium foil, (Bottom) Ratio of the $^{238}\text{U}(\gamma, f)$ and $^{238}\text{U}(\gamma, n)$ yields for offset from center to the left and down in uranium foil.	60
22 Neutron energy distribution in Both Foils for $B=8$, 14, and 20 MeV with respect to neutron fission cross section.	62
23 Neutron energy distribution in Uranium foil for $B=8$, 14, and 20 MeV with respect to ^{235}U neutron fission cross section.	63
24 FWHM vs. photon energy to determine input values for the MCNP6 Gaussian Energy Broadening (GEB) card.	66
25 Comparison between measured and MCNP6 simulated γ -ray spectra for ^{137}Cs , ^{60}Co , ^{133}Ba , and ^{152}Eu for ADC2.	67
26 Match of the energy efficiency of simulated γ -ray spectra to experimentally produced efficiency model.	68
27 Measured γ -ray spectrum of the Pb shot (Left), Bagged sample of the Pb shot used as in-hall detector shielding during experiment (Right).	69
28 Summation of in-hall cycle measurements parsed from 2 to 112 s ^{232}Th and ^{238}U at $B=8$, 14, and 20 MeV from 0-500 keV (top left), 500-1000 keV (top right), 1000-1500 keV (bottom left), and 1500-2000 keV (bottom right).	70
29 Short-lived CFPY of ^{238}U at all three energies with respect to the multimode-fission model fit to ENDF-B/VII.0 fast and DT neutron fission fractional mass yields.	77
30 Short-lived CFPY of ^{232}Th at all three energies with respect to the multimode-fission model fit to ENDF-B/VII.0 fast and DT neutron fission fractional mass yields.	78
31 Short-lived CFPY of ^{238}U at endpoint energies 20 MeV (top), 14 MeV (middle), and 8 MeV (bottom) with respect to the multimode-fission model fit to ENDF-B/VII.0 fast and DT neutron fission fractional mass yields.	81
32 Short-lived CFPY of ^{232}Th at endpoint energies 20 MeV (top), 14 MeV (middle), and 8 MeV (bottom) with respect to the multimode-fission model fit to ENDF-B/VII.0 fast and DT neutron fission fractional mass yields.	82

LIST OF TABLES

<u>Table</u>	
	<u>Page</u>
1 Mass and Geometry of Samples from Cycling Experiment	26
2 ICP-MS Isotopic Analysis of Uranium Foil	27
3 ICP-MS Isotopic Analysis of Thorium Foil	28
4 ICP-MS Trace Element Analysis of Uranium and Thorium Foils . .	30
5 Accelerator Parameters and Excitation Energy for Each Target . .	33
6 γ -rays Included in HPGe Energy Efficiency Model	38
7 Photofission Events Per Pulse	64
8 Photofission Product Yields for ^{238}U at $\langle E^*(B) \rangle = 12.59 \pm 0.01 \text{ MeV}$.	71
9 Photofission Product Yields for ^{238}U at $\langle E^*(B) \rangle = 10.30 \pm 0.01 \text{ MeV}$.	72
10 Photofission Product Yields for ^{238}U at $\langle E^*(B) \rangle = 6.78 \pm 0.01 \text{ MeV}$.	73
11 Photofission Product Yields for ^{232}Th at $\langle E^*(B) \rangle = 11.50 \pm 0.03 \text{ MeV}$.	74
12 Photofission Product Yields for ^{232}Th at $\langle E^*(B) \rangle = 9.22 \pm 0.01 \text{ MeV}$.	75
13 Photofission Product Yields for ^{232}Th at $\langle E^*(B) \rangle = 6.74 \pm 0.02 \text{ MeV}$.	76

Short-lived Photofission Product Yields and Analytical Methods for Nuclear Forensic Application

1 Introduction

Fission remains a phenomenon of ongoing interest and continues to receive substantial attention as an area of research within the nuclear nonproliferation, forensics, and safeguards communities. These national and homeland security applications, as well as others, such as nuclear waste transmutation and reprocessing [1], electron accelerator-based high-flux neutron source design and development [2], and accelerator-driven subcritical reactor design [3], require consistent and reliable fission data. However, the majority of the existing photonuclear data relies on nuclear models; published experimental measurements performed to date are somewhat limited and often inconsistent. Despite decades of previous research, many aspects of the available, empirical fission data are lacking. As a consequence, the evaluated data widely used by computational tools suffer from inaccuracies and large relative uncertainties, particularly with respect to short-lived and low-yield fission products.

A variety of high-energy particles can excite a nucleus and cause fission in nuclear materials. Although neutron fission is the main interest of nuclear reactor physics, fission induced by high-energy photons is also studied, but more frequently in the context of fundamental physics or national security applications [4]. Induced fission experiments have long been done with linear accelerator-produced bremsstrahlung X-rays to study high-energy photon-induced fission, known as “photofission” [5, 6].

The initial fission process and the subsequent decay of fission products produce

signals, including prompt and delayed neutrons and γ -rays, can be measured for detection and identification purposes. Delayed γ -rays are less difficult to detect following a fission event due to their abundance and duration, when compared to delayed neutrons [4]. A unique γ -ray distribution exists due to the decay of fission products and products of alternative reactions for each fissionable isotope, which may be measured using γ -ray spectroscopy to aid in material identification [4]. The yield of individual fission products can be determined from analysis of γ -ray spectra, leading to identification of the source through the fission product yield distribution. The work in this thesis aims to measure short-lived fission product yield distributions of photon-induced fission of two actinides, ^{238}U and ^{232}Th , at multiple excitation energies.

1.1 Motivation

This work is motivated by a demonstrated need for novel isotope production methods for nuclear forensics and improved nuclear data to support the nonproliferation community [7]. Nuclear forensics is the science of characterizing nuclear materials through analysis techniques such as radiochemical analyses and radiation detection methods, with the intent to attribute of the material to its origin and process history. This attribution process is intended to be performed within the context of law enforcement investigations, and therefore requires chain of custody matched to traditional forensics for use in prosecution [8]. When this material characterization is performed in conjunction with forensics databases and information from intelligence agencies, the nuclear forensics analysis can potentially indicate the place of origin or device type [9].

The fission product yield distributions are dependent on the energy of the

incident particle and the mass of the target nucleus, but generally reflect the shape of a double-humped curve, with low and high mass “peaks” and an intermediate mass “valley”. As the energy of the incident particle increases, the excitation energy of the nucleus increases, and the isotopes in the valley increase in overall yield with respect to the two maxima or peaks of the fission product curve [8]. In post-detonation nuclear forensics, the peak-to-valley ratio of the fission product curve could be used for characterizing device type by providing an indication of the neutron energy spectrum that had induced fission (*e.g.*, 500 keV vs. 14 MeV) [8]. Photofission is most probable for incident photons around 14 MeV due to the giant dipole resonance; induced photofission around this energy results in a fission product yield distribution that resembles DT 14 MeV neutron fission more than thermal or fast (500 keV) neutron fission. A less costly and more flexible production method for these valley isotopes that are representative of DT neutron fission product yield distributions would benefit nuclear forensics exercises in testing for analysis techniques.

1.2 Objectives

The goal of this work is to improve nuclear data for isotopes of interest in nuclear forensics and special nuclear material (SNM) detection. Improvement of nuclear data will be achieved by adding to the body of empirical data on photofission product yields. The objectives listed below will allow this goal to be achieved.

- Measure short-lived ($T_{1/2} \leq 50$ s) photofission product yields of ^{238}U and ^{232}Th at endpoint energies of 8 MeV, 14 MeV, and 20 MeV.
- Perform thorough uncertainty analysis to ensure uncertainty can be confidently declared.

- Develop experimental and analysis methods for consistent future photofission product yield measurements of additional fissional nuclides and endpoint energies.

1.3 Document Overview

Chapter 2 - Background and Theory

Background information is introduced on the mechanics of photon-induced fission, the analysis of fission products, relevant nuclear forensics signatures, and the history of the high-throughput detection methods of γ -ray spectroscopy employed.

Chapter 3 - Materials and Methods

A description of the full experimental setup and methodology. Included are the target compositions, parameters of the linear accelerator, the pneumatic transfer system, and the γ -ray spectroscopy instrumentation. The analytical methods used in determining the fission product yields are described.

Chapter 4 - Simulation and Characterization

Simulation and characterization of all components of the experiment are described. This includes: simulation of the bremsstrahlung spectra, photon and electron flux on target, HPGe detector response, and consideration of the uncertainty in the calculated number of fissions.

Chapter 5 - Results

The measured short-lived cumulative fission product yields for ^{232}Th and ^{238}U are reported. Results are compared with the body of published data where available.

Chapter 6 - Conclusions and Future Work

Conclusions from the resulting short-lived photofission products are discussed.

Future work in the area is proposed.

2 Background and Theory

2.1 The Photofission Process

Fission is the process of an excited nucleus transforming into a more stable state by splitting into smaller nuclei, resulting in an increase of the binding energy per nucleon of the fission products. The process of fission may occur as a spontaneous decay process in heavy nuclei, or as the result of an incident particle interacting with a nucleus and imparting sufficient energy to cause fission. High-energy (MeV) photons can induce fission, known as “photofission”, when the photon energy is high enough to overcome the first fission barrier [10].

A simplified description of the stages of the fission process are excitation, deformation, and scission. During the excitation stage, the excitation energy of the nucleus—the “compound nucleus” after absorption of an incident particle—is equal to the sum of the binding energy of the incident particle and its kinetic energy [11]. Most of the excitation energy of the compound nucleus manifests as deformation energy, splitting the nucleus apart [10]. As the nucleus deforms, there is an increase in potential energy. As the nucleus continues to deform or “stretch” along one axis, fission occurs with certainty once a point of critical deformation is reached [8]. The Coulomb forces of each end of the deformed nucleus repel one another, and a thin neck is formed, preserving the parts in a single nucleus. The break at this neck, the scission point, of the deformed nucleus is called scission. The fission fragments are then released from one other, reaching 90% their maximum kinetic energy within 10^{-20} s [8].

The time-scale of the prompt and delayed emissions following fission can be seen in Figure 1. In Figure 1, the time $t=0$ refers to the time the incident photon

is absorbed by the nucleus. The time of the fission event with respect to absorption, 10^{-20} s, is given, along with the time of the prompt and delayed emissions. Fission fragments may emit prompt neutrons and prompt γ -rays, which occurs within the first 10^{-13} seconds following fission [4]. The delayed emissions include neutrons, β^- particles, neutrinos, and γ -rays, which are described in more detail in following sections. The average total energy released during a fission event is about 200 MeV, which includes the energy of emitted particles and the kinetic energy of the fission products [10, 12].

One benefit of photofission experiments, when compared to neutron-induced fission, is the ability to investigate fundamental physics of fission at excitation energies lower than is possible with neutrons [10]. In neutron-induced fission, absorption of the incident neutron results in a compound nucleus with an excitation energy at least equal to the neutron binding energy; thus, the lowest energy region of the fission barrier can not be studied [13]. With photon-induced fission, a much broader range of excitation energies can be studied. Photons, like neutrons, have the benefit above charged particles in inducing fission as there is no coulombic interaction with the target nuclei. Furthermore, photofission studies have the benefit of highly penetrating, high-energy incident photons that allow for the use of thicker targets in experiments, despite the relatively low cross section for photofission when compared to the average neutron-induced fission cross section for many heavy nuclei [10].

Experimental data on photofission are scarce and often difficult to evaluate as a set due to differences in experimental setup and photon source energy distribution. As a result, models are most often used as a replacement in practical applications [14]. Models that rely on neutron-induced data assume that after absorption

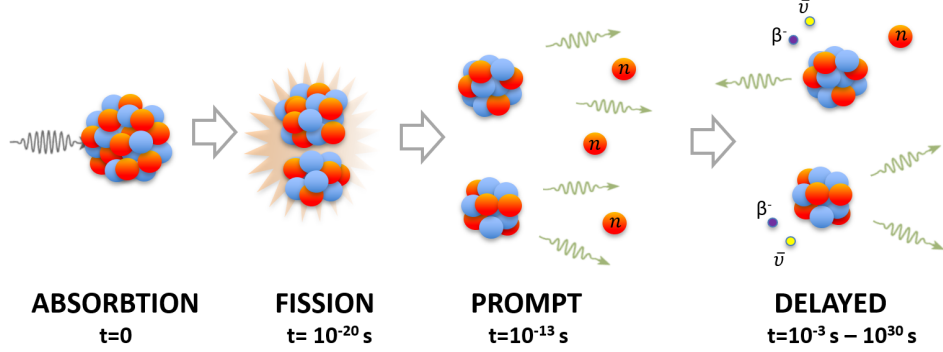


Figure 1: Time scale and description of both absorption, fission, and finally the prompt and delayed emissions following photon-induced fission.

of the incident particle, the excited nucleus will fission independent of its formation process. Using such models, the excitation energy of the nucleus and the mass of the target nucleus must be known. A limitation of these models is that the neutron separation energies and resulting Watt spectrum are needed when simulating photofission in this manner. For example, in the current version of MCNP6 and photofission data in ENDF/B-VII.0, this information is only available for 39 target actinides [15].

2.1.1 The Giant Dipole Resonance

Photoabsorption by the nucleus with γ -rays on the order of tens of MeV, is made possible by the giant dipole resonance (GDR). GDR is a broad resonance that ranges from about 6 MeV to 30 MeV for heavy nuclei and at 20 MeV to 25 MeV for light nuclei. [16,17]. The GDR is an oscillation of the protons and neutrons in opposite directions along the same axis within the nucleus. This movement of protons against neutrons produces an electric dipole field and corresponds to the fundamental frequency for absorption of electric dipole radiation for the nucleus as a whole [16]. For photofission of actinides, the GDR is most probable around 14

MeV, when the wavelength of an incident photon is on the same order of magnitude as the size of the nucleus [6, 15, 17].

The shape of the photoabsorbtion cross section is influenced by the deformation state of the nucleus. For quadrupole-deformed nuclear states that have an elongated and shortened shape along different axes of deformation, the oscillation of protons and neutrons along the “long” and “short” axes results in the lower energy and higher energy local maxima resonance peaks in the photoabsorbtion cross sections respectively [16, 17]. The results of these high and low peaks from the GDR are reflected in the shape of several of the photofission cross sections and can be seen in Figure 2. Figure 2 is a comparison of all the evaluated photofission cross section data for actinides in ENDF-B/VII.0. No error information is given in ENDF-B/VII.0 for these photofission cross section evaluations.

2.1.2 Multimode-Fission Model

In the mutlimode-fission model, the mass distributions of fission products is understood by the sum of three separate fission modes. These three fission modes are known as a symmetric superlong mode (SL) and two asymmetric modes, standard I and II (STI and STII). These fission modes are the result of several passages through the fission barrier, resulting in a different combination of fission product mass distributions. Asymmetric fission is the dominant fission mode at low excitation energies and is characterized by shell effects in the nucleus; symmetric fission of a nucleus is better described using the liquid-drop model and becomes the more probable fission mode with higher excitation energies [18, 19].

The yield of three fission modes can be modeled as the sum of five Gaussian peaks, one for the symmetric mode and two for each asymmetric mode (for the

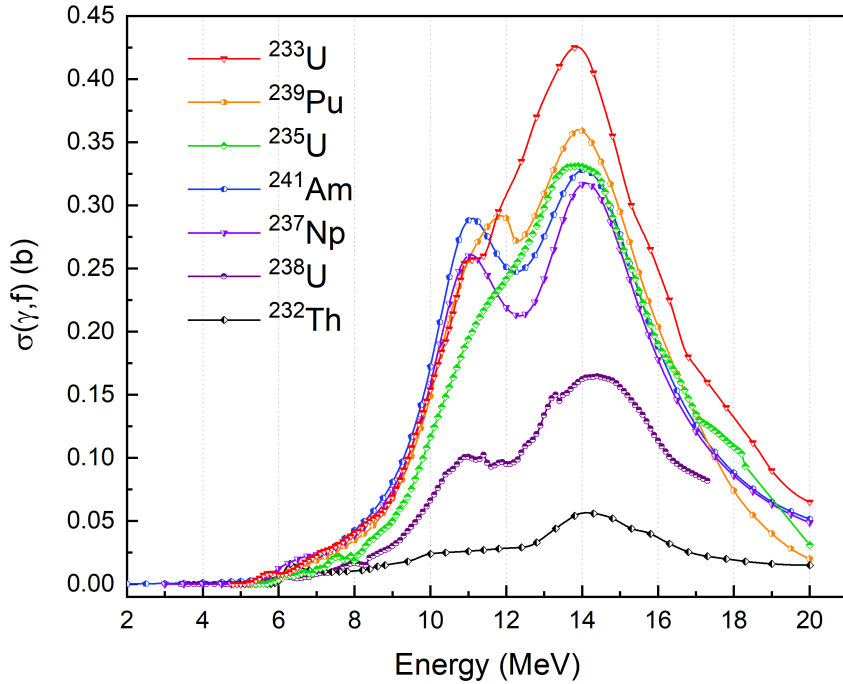


Figure 2: Compilation of ENDF-B/VII.0 evaluated cross $\sigma(\gamma,f)$ for actinide targets.

low and high mass peaks). Equation (1) outlines the summation of the three modes used in this multimode-fission model and Equation (2) includes all necessary parameters for modeling the five Gaussian peaks. Although this model has been used in studies of neutron-induced fission, not until recent years has the energy dependence of fission modes for photofission been studied [14, 18–20].

$$Y(A) = Y_{SL}(A) + Y_{STI}(A) + Y_{STII}(A) \quad (1)$$

$$\begin{aligned}
Y(A) = & K_{SL} \cdot \exp \left[-\frac{(A - \bar{A}_{SL})^2}{2\sigma_{SL}^2} \right] + \dots \\
& K_{STI} \cdot \exp \left[-\frac{(A - \bar{A}_{SL} - D_{STI})^2}{2\sigma_{STI}^2} \right] + \dots \\
& K_{STI} \cdot \exp \left[-\frac{(A - \bar{A}_{SL} + D_{STI})^2}{2\sigma_{STI}^2} \right] + \dots \\
& K_{STII} \cdot \exp \left[-\frac{(A - \bar{A}_{SL} - D_{STII})^2}{2\sigma_{STII}^2} \right] + \dots \\
& \dots K_{STII} \cdot \exp \left[-\frac{(A - \bar{A}_{SL} + D_{STII})^2}{2\sigma_{STII}^2} \right] \quad (2)
\end{aligned}$$

In (1) and (2), A is the mass of the fission product being evaluated; \bar{A}_{SL} is the most probable mass value for the symmetric fission mode; $\bar{A}_{SL} - D_{STI}$ and $\bar{A}_{SL} + D_{STI}$ are the most probable masses of the light and heavy fission products in the STI mode; $\bar{A}_{SL} - D_{STII}$ and $\bar{A}_{SL} + D_{STII}$ are the light and heavy peaks for the STII mode; K_{SL} , K_{STI} , and K_{STII} are the amplitudes of the Gaussian peaks for each respective mode; and σ_{SL} , σ_{STI} , and σ_{STII} are the widths of the respective Gaussian peaks. Equation (2) calculates the contributions of each fission mode when fitting to a fission product yield curve [18].

Figure 3 is a graphical representation of the multimode-fission model using Equation (2) to fit the five Gaussian distributions to the neutron-induced ENDF-B/VII.0 fractional mass yields of ^{238}U and ^{232}Th . Here, the multimode-fission model was fit to fast (500 keV) and high-energy (14 MeV) fission to compare how the excitation energy of the target nucleus affects the distribution from the three fission modes. The excitation energies of the 500 keV neutron fission are 5.30 MeV and 5.29 MeV for ^{238}U and ^{232}Th respectively, while the excitation energies are 18.80 and 18.79 MeV respectively for 14 MeV neutron fission. With increasing

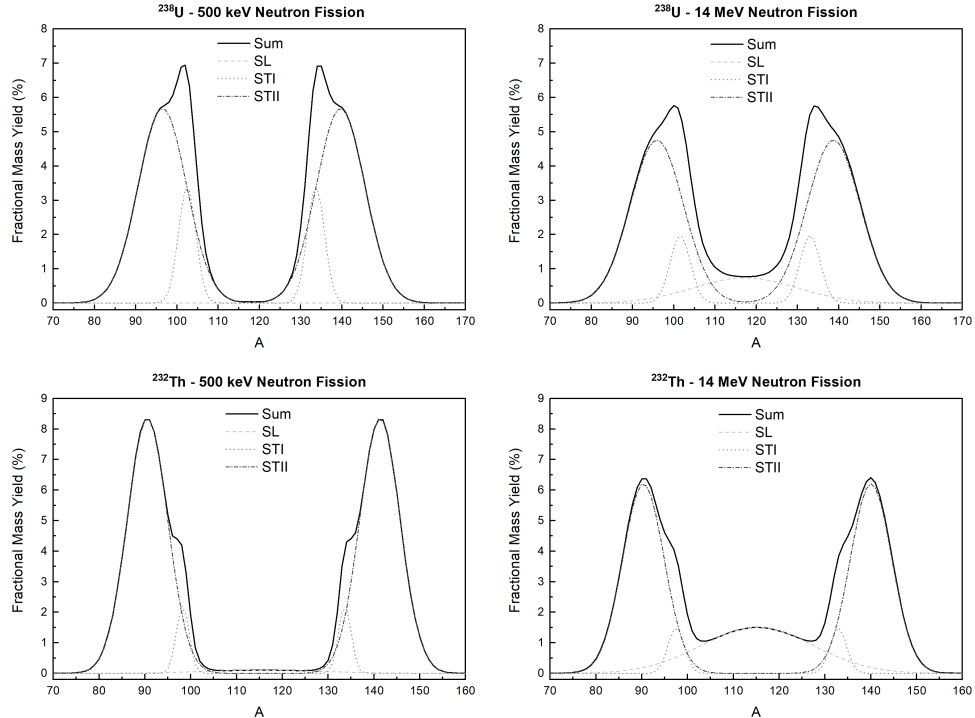


Figure 3: Fit of the SL, STI, and STII fission modes using five Gaussian peaks applied to ENDF-B/VII.0 fractional mass yield data for fast (left) and DT (right) neutron fission of ^{238}U (top) and ^{232}Th (bottom).

excitation energy, the contribution of the symmetric (SL) mode increases, as previously stated, with a decrease in the contribution of the asymmetric modes (STI and STII). The relative intensity of the STI and STII modes produces different shapes of the peaks for ^{238}U and ^{232}Th : ^{238}U having a higher STI intensity with respect to ^{232}Th , for example. This results in characteristic shapes of their respective high and low mass peaks, becoming more distinct at lower excitation energies.

The ratio of the maximum of the peaks (dominated by the asymmetric fission modes) to the yield of the fission products in the valley (dominated by the symmetric mode) is known as the peak-to-valley ratio. The maximum typically occurring at the maximum of the STI peaks and the valley at the portion of the curve dom-

inated by the SL symmetric mode. [18] The decrease in peak-to-valley ratio with increasing excitation energy is caused by a relative increase in the symmetric (SL) mode of fission. Although there is no standardized way to calculate the peak-to-valley ratio, an example calculation for ^{238}U is the ratio of the A=140 over the A=117 average mass chain yields, as stated by Beleshev *et al.* [14]. In a recent publication, Pahlavani and Mehdipour [21] compared their theoretical model to published experimental photofission product yield data for ^{238}U , ^{232}Th , ^{237}Np , and ^{240}Pu . The published data and the model were in good agreement regarding the decrease of peak-to-valley ratio in the fission product yield curve with increasing excitation energies of the ^{238}U nucleus.

In a study comparing these fission modes in both neutron- and photon-induced fission by Niak *et al.* [22], the peak-to-valley ratios, as well as the average heavy and light masses, were studied at various excitation energies. The authors found that with increasing excitation energy, the average value of the light mass peak decreases for the $^{238}\text{U}(\gamma, f)$, reaction while conversely increasing for the $^{238}\text{U}(n, f)$ reaction. The heavy mass peak showed an opposite trend due to conservation of mass. This suggests that in the fission by neutrons and photons, the symmetric and asymmetric modes may have different distributions for comparable excitation energies of a target nucleus [22].

2.2 Fission Products

Following the fission process, approximately 85% of the fission energy manifests as kinetic energy of fission products, useful for nuclear power generation, but not necessarily for radiation detection and the characterization of nuclear materials. Emissions from fission products, which include prompt and delayed neutrons and γ -rays, β particles, and neutrinos, are useful in the characterization of nuclear

materials. On average, a fission event results in 2 fragments that are neutron-rich—far from the line of stability. Those that are produced with the highest number of neutrons with respect to protons typically have the shortest half-lives (milliseconds to seconds). The decay processes of fission fragments, where excess energy is released to achieve a more stable state, is the reason for such high radioactivity of fission products [4, 13].

Along with β^- -decay—the predominant decay mode of fission products— γ -rays are frequently emitted with characteristic energies of the decaying nuclide. These characteristic γ -rays are known as delayed γ -rays. For a single fission event, an average of six to eight delayed γ -rays are emitted [4]. Delayed γ -rays are electrically neutral and 500 to 700 times more abundant than delayed neutrons. A complication in the measurement of short-lived fission products via delayed γ -rays is the high-rate of emission and the resulting paralysis of standard detection setups. The fission γ -ray spectra are much more complicated before the short-lived products decay away, minutes to hours after irradiation [4, 23].

Fission product yields are often reported as either cumulative or independent yields. The independent yield is the yield of that nuclide exclusively from the initial fission event. Cumulative yields are the total yield of an individual nuclide, from both direct production by fission and decay of other fission products. Since it can be challenging to separate contribution directly from fission and from the decay of other nuclides, independent yields are difficult to measure. Without knowledge of multiple cumulative yields in the same decay scheme, it is nearly impossible to determine the independent yields of fission products. The independent yields and half-lives for the fission products in mass chains $A = 83\text{-}93, 95, 97, 99, 103, 105, 106, 125, 131\text{-}133, 137, 140, 141, 144, 147, 149$, and 151 are considered to

be the most important in determining the whole of the radioactive decay schemes of all fission products resulting from a fission event [24]. Additionally, the fission products in these mass chains contribute the most to the activity of the fission products for the first 10 days following a fission event. Despite this fact, there remains a lack of available experimental data on the independent yields of these nuclides [20, 24].

2.3 High-Energy Photon Sources

For the most straightforward studies in photofission, one would require a high-energy photon source with a monoenergetic photon beam that functions over a large range of energies. Since the beginning of the research on photonuclear interactions, experiments have primarily been carried out using bremsstrahlung X-rays, with a continuum of photon energies [6,10,16]. Studies have also used high-energy photons produced by nuclear reactions, such as the 17.5 MeV γ -rays from the $\text{Li}^7(p,\gamma)\text{He}^4$ reaction [25]. Limitations of sources relying on nuclear reactions include the fixed energy and limited flux [16]. Other methods for producing beams of monoenergetic photons are positron annihilation in-flight and tagged bremsstrahlung, but have limited ranges of energy that may be used [6, 26].

2.3.1 Yield from Bremsstrahlung Source

The use of a broad-band bremsstrahlung X-ray beam makes the study of photonuclear interactions at very specific energies difficult. To calculate the yield of any photonuclear reaction, the flux and energy spectrum from a bremsstrahlung X-ray source must be thoroughly characterized [27]. The number of photofission events as a result of being induced by a bremsstrahlung X-ray beam with endpoint energy B is given by

$$Y(B) = N_T \int_0^B \frac{dC(B, E)}{dE} \sigma_{\gamma,f}(E) dE, \quad (3)$$

where C is the number of photons at energy E , N_T is the number of atoms in the target, and $\sigma_{\gamma,f}(E)$ is the photofission cross section at energy E [27, 28]. This yield equation may be used to determine the reaction rate for any photonuclear reaction from a bremsstrahlung X-ray beam by substituting the appropriate cross section.

2.3.2 Excitation Energy from Bremsstrahlung X-Rays

Much of the published photofission product yield data are often reported relative to the bremsstrahlung X-ray endpoint energy; however, the average excitation energy of the fissioning nucleus is useful for comparison of experimental fission product yields and to fission induced by other particles. Even with the same endpoint energy, the use of different converter targets, operating parameters, and geometry of the experimental setup for the production of those bremsstrahlung X-rays will produce a different photon spectrum in the incident beam. Using an average excitation energy of the target nucleus rather than endpoint energy of the bremsstrahlung spectra allows for more reliable comparison among photofission experiments using bremsstrahlung X-rays [14, 18, 20–22].

The average excitation energy of a target nucleus during a photonuclear event is given as

$$\langle E^*(B) \rangle = \frac{\int_0^B \frac{dC(B, E)}{dE} \sigma_{\gamma,f}(E) E dE}{\int_0^B \frac{dC(B, E)}{dE} \sigma_{\gamma,f}(E) dE}, \quad (4)$$

where B is the energy of the electron beam from the linac, E is the incident photon energy, $\sigma_{\gamma,f}(E)$ is the photofission cross section, and $C(B, E)$ is the number of

photons of energy E in the bremsstrahlung photon spectrum [14, 20]. Since the average excitation energy is a function of photofission cross section, the excitation energy for a specific endpoint energy will differ for different target nuclides. The energy distribution of bremsstrahlung X-rays, $C(B, E)$, may differ depending on the experimental setup, despite comparable endpoint energies and target nuclides.

2.4 Interaction of Photons with Matter

Transmission and attenuation in matter is especially important in the measurement of photons. The two modes of attenuation of photons are scattering and absorption, which both contribute to the mass attenuation coefficient, μ . The attenuation of photons is most dependent on the energy of the photon, the density of the attenuating material, and the atomic number of the material. Due to the relatively low energy (keV-MeV) of emitted photons, the attenuation is primarily through Compton scatter. At energies greater than 5 MeV, loss through photonuclear processes (absorption and fission) becomes more dominant [4].

Quantifying the transmission of a mono-directional, mono-energetic photon beam through matter is given by

$$\frac{A}{A_0} = e^{-\mu\rho x}, \quad (5)$$

where A is the intensity of the transmitted photon beam, A_0 is the initial intensity of the photon beam, μ is the mass attenuation coefficient (with coherent scattering) in $\frac{\text{cm}^2}{\text{g}}$, ρ is density in $\frac{\text{g}}{\text{cm}^3}$, and x is the material thickness in cm.

Given the same mono-directional, mono-energetic photon beam, in situations where photons are emitted at any point (x) distributed throughout an attenuating material,

$$A_p = \frac{\int_0^\xi e^{-\mu\rho x} dx}{\xi}, \quad (6)$$

is used to determine the fraction of photons that transmit through the material, A_p , where ξ is the thickness of the foil in cm. The form of (6) differs from (5) as it considers photons emitted at points distributed throughout the material thickness, not just traveling through the full thickness. This is a one-dimensional simplification of the attenuation.

Photon interactions contributing to the total attenuation coefficient are coherent scattering, photoelectric effect, Compton scattering, and pair production. The summation of each of these contributions is given by

$$\mu(E) = \tau(E) + \sigma(E) + \kappa(E), \quad (7)$$

where $\mu(E)$ is the total attenuation coefficient (with coherent scattering), $\tau(E)$ is the coefficient for attenuation from the photoelectric effect, $\sigma(E)$ is the coefficient for attenuation through Compton scattering and $\kappa(E)$ is the coefficient for attenuation through pair production. These photon interactions are described in the following subsections.

2.4.1 Photoelectric Effect

The photoelectric effect is the release of a photoelectron from an electron shell of an atom, caused by photons being absorbed by an atom, and is one of the most probable interaction with matter for low-energy (eV-keV) photons. This photoelectric interaction does not occur with free electrons, only those bound in an electron orbitals. Although dependent on incident photon energy, the most likely orbital for the released photoelectron is the K-shell, the most tightly bound

of the electron orbitals [29]. The release of the photoelectron causes a vacancy in an orbital shell, so the vacancy is filled by a combination of absorption of a free electron and the rearrangement of outer shell electrons. This arrangement results in the emission of photons in the form of characteristic X-rays or an Auger electron releasing the excess excitation energy. The emitted photoelectron has an energy described by

$$T = h\nu - BE, \quad (8)$$

where T is the kinetic energy of the released photoelectron, BE is the binding energy of the electron from its original orbital shell, and $h\nu$ is the incident photon energy [4, 29].

2.4.2 Compton Scattering

Compton scattering is a scattering interaction between an incident photon and an orbital electron. This is the most probable photon interaction for photons in the keV to low MeV energy range [29]. An incident photon is scattered at an angle θ normal to its original trajectory and transfers energy with respect to the scattering angle to the target electron. Interaction probability of Compton scattering depends on the probability of interaction with an orbital electron and, therefore, interaction probability increases proportional to the atomic number, Z , of a target material [4]. The energy of the photon after Compton scatter is described by

$$E = \frac{E_0}{1 + \frac{E_0}{MC^2}(1 - \cos\theta)}, \quad (9)$$

where E is the energy of the scattered photon, E_0 is the energy of the incident

photon, MC^2 is the rest-mass energy of an electron, and θ is the scattering angle from the normal of the incident photon trajectory [4, 29]. In γ -ray spectroscopy, these Compton interactions are seen in the spectrum as a “Compton continuum,” a continuum of resulting photon energies from $\theta = 0^\circ$, where no photon energy is transferred, to $\theta = 180^\circ$, where the most photon energy is transferred via a single Compton scattering event [29].

2.4.3 Pair Production

Pair production is possible for photon with energies above 1.022 MeV, twice the rest-mass energy of an electron. Due to this threshold, pair production is primarily possible for high-energy (MeV) photons. In the process of pair production, the incident photon is replaced by an electron-positron pair after interaction with a nucleus. The incident energy of the photons up to 1.022 MeV is used in the creation of the electron-positron pair, and all energy above that is transferred to the kinetic energy of the pair as they are emitted opposite each other. The positron subsequently interacts with an electron, resulting in two 0.511 MeV annihilation photons. The two 0.511 MeV annihilation photons are emitted in opposite directions ($\theta=180^\circ$) [4, 29]. In γ -ray spectroscopy, pair production results in an annihilation peak at 0.511 MeV when one of the annihilation photons is absorbed in the active volume of the radiation detector [4, 29].

2.4.4 Photonuclear Absorption

The first published record of photonuclear absorption was in 1934, a paper in which Chadwick and Goldhaber described the reaction of deuterium interacting with ^{208}Tl γ -rays [30]. Once accelerators became more accessible for research in the 1950’s, photonuclear reactions began to be studied in more detail and for

nuclides that require photons with energy higher than what is available exclusively via radioactive decay [16].

The absorption of a photon by a nucleus results in an excited state. The nucleus de-excites through the prompt emission of particles such as photons, charged particles, or neutrons. The photonuclear reaction probability depends heavily on the incident photon energy. If the excitation energy of the nucleus following the absorption of a photon is higher than the binding energy, single or multiple nucleons may be emitted. This is the basis for photonuclear reactions such as (γ,n) , $(\gamma,2n)$, (γ,p) , and (γ,α) . With excitation energies below the binding energy for charged particles, elastic and inelastic scattering reactions such as (γ,γ) and (γ,γ') dominate [16].

2.5 High-Purity Germanium Detectors

High-purity germanium (HPGe) detectors are a type of semiconductor detector, often doped with controlled amounts of impurities and exhibit conductivity heavily dependent on temperature. In semiconductor detectors, charge transport is achieved through the movement of electron-hole pairs, similar to the function of electron-ion pairs in gas-filled detectors. Movement of electron-hole pairs in the active volume of the detector within the applied electric field generates a signal, proportional to the total energy deposition. Compared with sodium iodide (NaI), HPGe detectors have a much smaller cross section for the photoelectric interaction, causing intrinsic peak efficiency for HPGe detectors to be ten to twenty times lower than a NaI detector of the same volume. This results in much fewer counts under a full energy peak in the same measurements. However, these peaks are easier to deconvolve than those obtained with other detector types, as they are less likely to overlap due to their narrow peak widths (FWHM) [29, 31].

It is necessary to cool HPGe detectors because germanium crystals have an extremely small energy gap. Cooling prevents thermally generated charge carriers that reduce the resolution. At the required operating temperatures, about 77 K, thermally generated noise is not an issue and energy resolution remains superior to many other spectroscopic measurement devices [31]. Superior energy resolution is a consequence of the increased number of charge carriers when compared to other types of detectors [31].

An important limitation of semiconductor detectors is that they are particularly susceptible to radiation exposure damage. This occurs when an atom within the semiconducting material is displaced by an incident particle. A displaced atom could end up in an interstitial position and result in an interstitial-vacancy pair, known as a the Frenkel defect. These defects potentially lead to trapping electron-hole pairs and degradation of energy resolution. Depending on the type of semiconductor material, the most damaging radiation is different. For HPGe detectors, fast neutrons are the most damaging, while photons and electrons do not cause significant damage [29].

2.6 High-Rate Applications

One of the challenges associated with measuring low-yield, short-lived fission products is the inability of commercial detectors and data acquisitions systems to operate quickly, efficiently, and in high-flux environments, a necessity for these measurements. Similar detection requirements exist for practical security and safeguards applications relying upon observing fission signatures to detect and identify SNM. Increasing the throughput capabilities—the amount of information the acquisition system can process without loss—and limiting the processing time required

for those measurements is of paramount importance. Depending on the type of radiation measurement, the timing considerations for the detector setup vary. If the count rate is too high following the irradiation and paralyzes the detectors, the shortest-lived decay products may decay before the measurement can begin. In situations where delayed γ -ray spectra are measured to characterize the composition of a sample, a long irradiation is often followed by a comparable cooling period to prevent paralysis of the detector equipment. This follows a typical measurement of an irradiated sample where the isotopes of interest have a long enough half-life to be measured with confidence after the cooling period [4, 32–34].

For experiments where the very short-lived delayed γ -rays are not crucial to the analysis, but superior energy resolution is desired, HPGe detectors are often utilized in an auxiliary counting lab following irradiation and subsequent adequate cooling time. The cooling time allows for a sufficient decay of the shortest-lived fission products to reduce the dead-time of the HPGe detectors during the measurement. Since there is still a considerable signal intensity of samples long after induced photofission, the analysis of a sample using delayed γ -ray signatures often uses this approach [33].

To maximize the amount of information that can be extracted from a fission event, the ability to maximize count rates without losing energy resolution is a delicate balance. Immediately following an accelerator pulse, in a typical measurement the count rate could exceed 10^6 s^{-1} . The intensity of the produced signal has a prompt drop following the end of an individual accelerator pulse and a considerable amount of information is lost in a measurement that begins much later. It is preferred to start as early as possible to maximize the count contribution from short-lived fission products. This measurement scheme also needs to be optimized

so the system does not get overloaded causing extended dead time. The approach to the measurement of these also requires consideration of the active background and the timing between the pulses of the accelerator. These measurement techniques have been done in close proximity to linear accelerators and between the individual pulses [34–36].

2.7 Nuclear Forensics Applications

Part of the Nonproliferation Initiative of 1992 describes the need for the post-detonation determination of a device design from the resulting debris, the drive for the creation of the field of nuclear forensics [8]. As described in the prior sections, fission product yields reveal much about the fission process from which they were produced. Most generally, fission product yields are characteristic of the target nuclide, so decreasing uncertainty on experimental fission product yields benefits nuclear forensics very directly. The fuel type may be determined through the fission product yield contributions of one or more actinides. If a large portion of the fission product yield curve is measured following an event, it could be possible to determine contributions from more than one fuel type [9,37].

3 Materials and Methods

3.1 Introduction

In February and March 2018, experiments were performed at Idaho State University’s Idaho Accelerator Center (IAC) using their 25-MeV electron linear accelerator (linac). These experiments utilized an Ortec GMX series, mechanically-cooled HPGe detector. Detections of the delayed γ -rays emitted by photofission products from both ^{232}Th and ^{238}U were carried out during cycles between the irradiation by a bremsstrahlung X-ray beam with endpoint energies of 8, 14, and 20 MeV.

This chapter introduces the materials utilized in these experiments, including the targets, the linear accelerator, the pneumatic transfer system, the HPGe detector, and the list-mode data collection system. Analysis for verification of the materials used and assumptions made are described. The analytical methods used to calculate fission product yields from these data are included, with the uncertainty analysis carried out.

3.2 Description of Targets

Foils of ^{238}U and ^{232}Th were irradiated and analyzed to measure and compare photofission product yields. Targets were irradiated at multiple endpoint energies for a comparison of the photofission product yields based on excitation energy of the nucleus. ^{238}U was chosen because the most published experimental data for photofission product yields is available for this nuclide, potentially providing comparison with collected data [14,18,22,23,35,38–41]. Compared with ^{238}U , ^{232}Th has significantly less published experimental product yield data [19,42]. Another consideration is that, as a fertile material, proliferation concern is minimized in

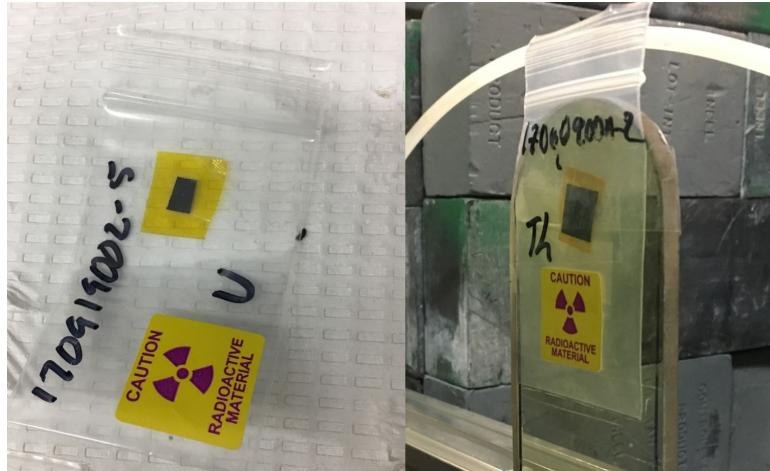


Figure 4: Uranium sample cut and secured in sample bag with teflon tape (left), Th sample as attached on sample holder of the pneumatic track (right).

the irradiation and handing of ^{232}Th .

3.2.1 Target Geometry

The ^{238}U and ^{232}Th foils were purchased from Goodfellow Corporation, with reported thicknesses of 0.178 mm and 0.125 mm, respectively. The original 11 mm by 17 mm ^{238}U was cut into smaller pieces. The ^{232}Th samples were cut from a 9 mm by 50 mm foil. The mass of each irradiated sample is provided in Table 1. As all samples were cut from the same original foils, the thicknesses of each individual sample of ^{238}U and ^{232}Th were assumed to be consistent.

Table 1: Mass and Geometry of Samples from Cycling Experiment

Nuclide	Endpoint Energy	Mass (g)	ρx ($\frac{\text{g}}{\text{cm}^3}$)	Thickness (mm)
^{238}U	8 MeV	0.1172	0.2739 ± 0.0013	0.1445 ± 0.0007
	14 MeV	0.1113		
	20 MeV	0.1133		
^{232}Th	8 MeV	0.1004	0.6644 ± 0.0009	0.0567 ± 0.0005
	14 MeV	0.1100		
	20 MeV	0.0990		

To verify reported thicknesses provided by the Goodfellow Corporation, the thickness of each individual foil was calculated with the density-thickness, ρx ($\frac{\text{g}}{\text{cm}^3}$), by measuring the transmission of ^{152}Eu γ -emissions through the foils. The density thickness was calculated by using Equation (5), which calculates the transmission of photons through a medium of thickness, x , using the attenuation coefficient, μ . The emission of ^{152}Eu γ -rays was measured from a bare, uncollimated source. Using the same source geometry, the foil was used to shield the ^{152}Eu source at centered, left-offset, and right-offset positions. The ratio of counts measured from the ^{152}Eu γ -rays of the shielded (I) to bare (I_0) was used. With the values for $\frac{I}{I_0}$ and μ known, using a nonlinear fit through the $\frac{I}{I_0}$ for each measured γ -ray, the value for density thickness, ρx was calculated. Using the known densities, ρ , for elemental uranium and thorium, 18.95 and 11.70 $\frac{\text{g}}{\text{cm}^3}$, respectively, the thickness, x , was found. The average of these three calculated thicknesses (centered, left, and right) is reported as the thickness in Table 1. The result of nonlinear least squares fitting for each position is given in Figures 5 and 6 for the uranium and thorium foils respectively. Attenuation coefficients (with coherent scattering), μ , of each measured ^{152}Eu γ -ray energies were extracted from the National Institute of Standards and Technology XCOM Photon Cross Section Database [43]. XCOM does not list the uncertainty on the mass attenuation constants. The foils could not be accurately measured using a caliper due to radioactive contamination concerns.

3.2.2 Target Composition

Table 2: ICP-MS Isotopic Analysis of Uranium Foil

Sample	$^{234}\text{U}(at.\%)$	$^{235}\text{U}(at.\%)$	$^{238}\text{U}(at.\%)$
U Foil	$0.0054\% \pm 0.0002\%$	$0.736\% \pm 0.009\%$	$99.26\% \pm 0.01\%$
Natural U Standard	$0.0055\% \pm 0.0002\%$	$0.720\% \pm 0.005\%$	$99.27\% \pm 0.01\%$

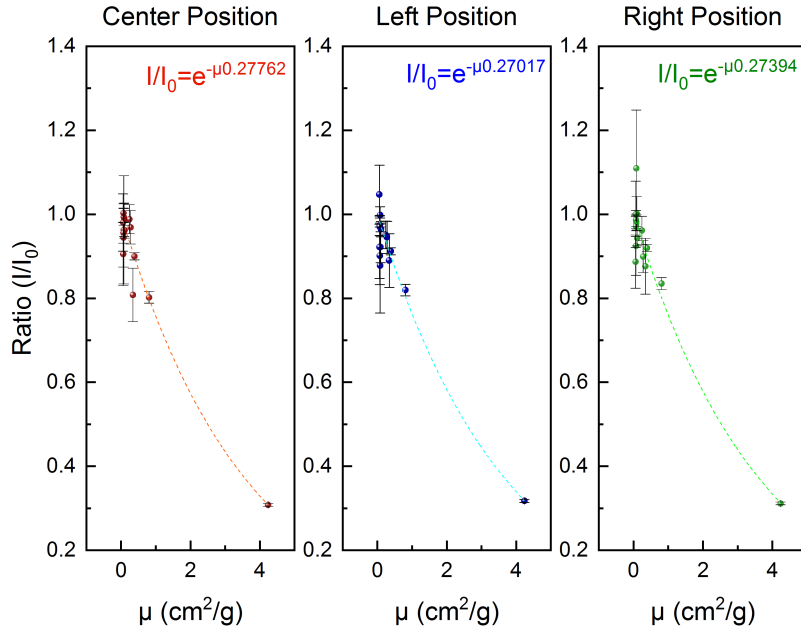


Figure 5: Attenuation of ^{152}Eu γ -rays in 0.1445 ± 0.0007 mm thick uranium foil fit to determine ρx ($\frac{\text{g}}{\text{cm}^3}$).

Table 3: ICP-MS Isotopic Analysis of Thorium Foil

Sample	$^{228}\text{Th}(at.\%)$	$^{229}\text{Th}(at.\%)$	$^{230}\text{Th}(at.\%)$	$^{232}\text{Th}(at.\%)$
Th Foil	$< 1 \cdot 10^{-4}\%$	$< 1 \cdot 10^{-4}\%$	$< 1 \cdot 10^{-4}\%$	$99.99992\% \pm 0.00002\%$

Isotopic analysis using inductively coupled plasma mass spectrometry (ICP-MS) was performed on small samples of the unirradiated uranium and thorium foils. The isotopic analysis of the uranium foil sample was compared against the NIST isotopic standard CRM-145 at both the end and the beginning of sample analysis [44]. The major isotopes of uranium for the uranium foil sample and the standard are listed in Table 2. The isotopic analysis of the thorium sample was calculated using intensity values from the ICP-MS. Table 3 lists the isotopic analysis of the thorium sample in atom percent. The contribution of thorium

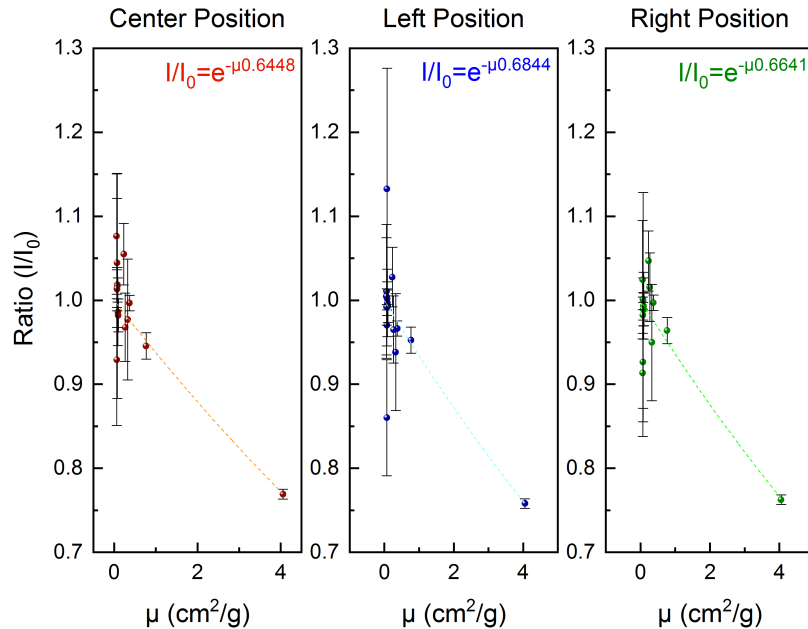


Figure 6: Attenuation of ^{152}Eu γ -rays in 0.0567 ± 0.0005 mm thick thorium foil fit to determine ρx ($\frac{\text{g}}{\text{cm}^3}$).

isotopes aside from ^{232}Th was less than $10^{-4}\%$. The ^{232}Th sample was analyzed using a gravimetric calibration curve of multi-element ICP-MS analysis to measure the trace elements in the thorium sample. Table 4 lists the elements that were detected in trace analysis in the uranium and thorium samples. For the uranium foil sample, only three elements were significantly above the limits of detection: cobalt, tin, and tungsten. Chromium, iron, manganese, nickel, molybdenum, and zinc were also found slightly above the limits of detection, although not listed in Table 4. It is likely that these latter elements are present as a result of stainless steel contamination during the preparation of the foil samples.

Table 4: ICP-MS Trace Element Analysis of Uranium and Thorium Foils

Sample	Trace Element	Concentration ($\frac{\text{mg}}{\text{g}}$)
U Foil Sample	Co	42±7
	Sn	150±30
	W	34±7
Th Foil Sample	Te	210±40
	Zn	11.4±0.3

3.3 In-Hall Experimental Setup

The experiment was performed using a cycling experimental setup. This setup utilized a pneumatic transfer system to repeatedly move the irradiated sample from the irradiation position to the HPGe detector face and rapidly back. The measurement instrumentation was set up within the linear accelerator hall (linac hall) that houses the 25 MeV and 44 MeV electron linear accelerators at the Idaho Accelerator Center. The HPGe detector was heavily shielded with lead bricks, lead shot, polyethylene detector housing the detector fit inside, and additional polyethylene bricks to prevent damage from scattered radiation around the linac hall.

Figure 7 is a photograph compilation of the full in-hall experimental setup for the cycling experiment. On the right of Figure 7, the irradiation end is shown. The close-up figure in the right corner shows a bagged thorium sample attached to the sample holder. As seen here, prior to irradiation, samples were aligned with a laser to center them within the incident photon beam. The sample was held at the front end of the sample holder on the pneumatic track, 8.1 cm from the downstream face of the aluminum beam scrub. The left side of the figure shows the detector end of the experimental setup. Behind the polyethylene bricks, the detector was housed in a cubic polyethylene housing with lead rings that fit snugly around the HPGe

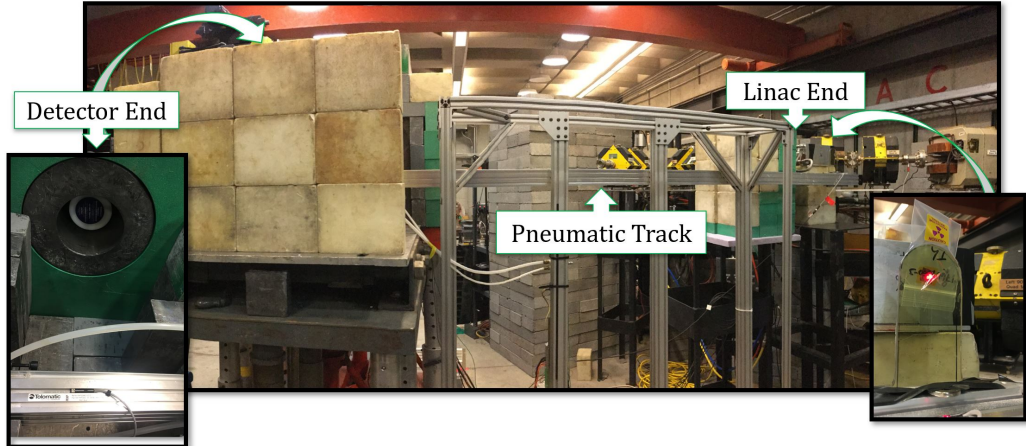


Figure 7: Photograph of full in-hall experimental setup at the Idaho Accelerator Center (middle), view of detector end of the pneumatic track (left), linac end of the pneumatic track showing sample placement (right).

detector. The left corner of Figure 7 shows the HPGe detector face with respect to the lead rings, polyethylene housing (green), and pneumatic track.

3.3.1 25 MeV Linear Accelerator

Electron linear accelerators accelerate electrons along a straight trajectory by means of an electric field produced by high-frequency oscillating voltage. A electromagnetic wave “travels” along the metallic cylinder, known as the waveguide. This wave carries the electrons— injected at the origin by an electron gun— through the length as they are continuously accelerated. Within an internal vacuum tube, the electron beam moves through a series of alternating conductive electrodes with small holes for the charged particles to pass. The klystron produces the required high-frequency oscillating voltage that accelerates the particles as they move from one electrode to the next. As electrons move from one electrode to another, those in phase are accelerated during the half-phase when the electric field is in the position that allows for acceleration in the desired direction. During the other half-phase, the electrons are shielded inside hollow metal conductive electrodes [11, 45]. When

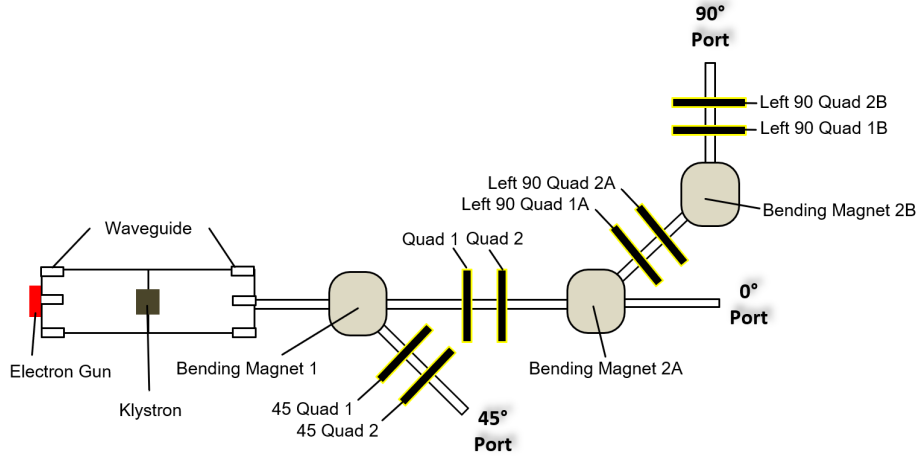


Figure 8: Schematic of the 25 MeV Electron Linear Accelerator at the Idaho Accelerator Center.

used as a photon source, high-energy electrons escape the end of the linac, and impinge upon a high-Z radiator. The radiator is used to convert an energetic electron beam to a photon beam through bremsstrahlung. Bremsstrahlung is the process of electrons releasing their kinetic energy as photons during deceleration when deflected by the electric field of target nuclei [11].

The high-energy photon beam used to induce photofission was produced with the 25 MeV linear electron accelerator at Idaho State University's Idaho Accelerator Center. Figure 8 is a schematic of the primary components in the 25 MeV linac at the IAC, including those described previously as well as dipole and quadrupole magnets (quads). The dipole magnets are used to bend the electron beam at an angle, necessary for the 45 and 90 degree ports. The quads are used to focus the beam and prevent spread as the beam travels to the individual ports. The 25 MeV linac has an output electron energy range from 4 to 25 MeV, a pulse width from 50 ns to 4 μ s, and a repetition rate, $1/\tau$ (where τ is the period (s)), from 1 to 360 Hz [46]. The output electron energy is the highest energy for bremsstrahlung X-rays. The repetition rate is the number of pulses per second output by the linac,

Table 5: Accelerator Parameters and Excitation Energy for Each Target

Target	B (MeV)	$\langle E^*(B) \rangle$ (MeV)	$1/\tau$ (Hz)	Cycles	$Q_{Average}$ (nC)
^{238}U	8	6.78 ± 0.01	200	50	361.39 ± 2.88
^{238}U	14	10.30 ± 0.01	15	50	186.73 ± 1.26
^{238}U	20	12.59 ± 0.01	2	50	302.42 ± 1.20
^{232}Th	8	6.74 ± 0.02	200	60	257.90 ± 1.22
^{232}Th	14	9.22 ± 0.01	30	60	190.01 ± 1.35
^{232}Th	20	11.50 ± 0.03	6	50	303.36 ± 1.64

with pulse width referring to the duration of an individual pulse. These parameters are all adjusted and optimized for individual experiments. In this work, “cycles” refers to the number of irradiations and detector measurements done in sequence for the individual nuclide/endpoint energy pair. The beam charge was measured by a Pearson Current Monitor at the electron beam exit point. This charge was measured for each individual irradiation cycle and averaged over each experiment, $Q_{Average}$. The accelerator parameters for each of the in-hall cycling measurements are reported in Table 5. The pulse width was consistent for all irradiations at 4 μs . The excitation energy of each target was calculated using Equation (4), a function of the target nucleus and incident photon beam.

Figure 9 shows the simulated bremsstrahlung X-ray spectrum for the three endpoint energies 8, 14, and 20 MeV, with the photon fluence value given on the right y-axis. The photofission cross sections for both ^{238}U and ^{232}Th are pictured for the same energy range, with the value on the left y-axis. The maximum of both (γ, f) cross sections occurs around 14 MeV.

3.3.2 Pneumatic Transfer System

Figure 10 shows the layout of the sample geometry during irradiation and subsequent counting. The pneumatic transfer system was 105 cm in travel length,

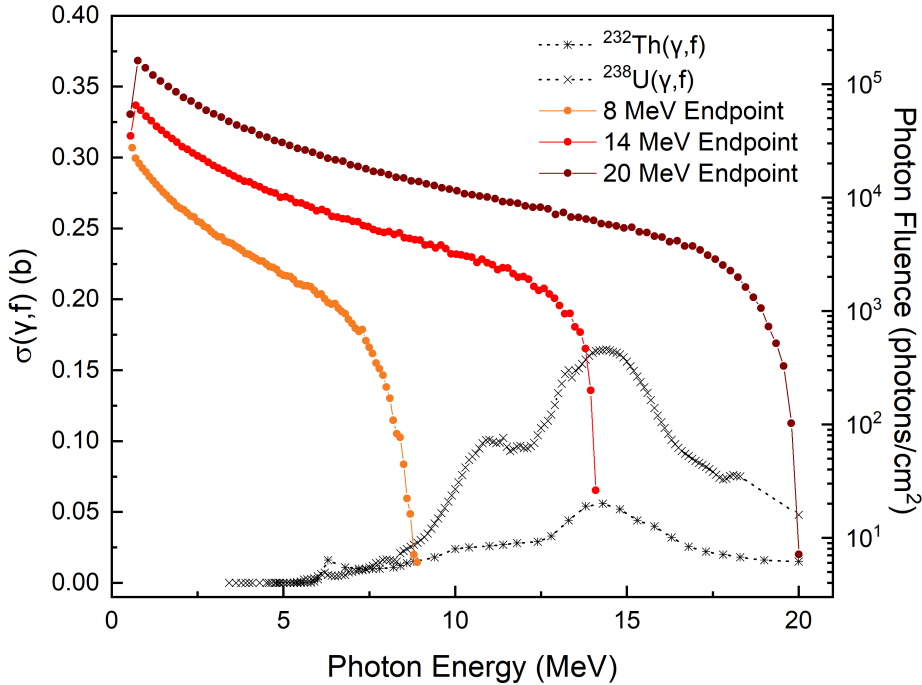


Figure 9: Simulated bremsstrahlung X-ray flux incident on target at 8, 14, and 20 MeV endpoint energies (right axis) with reference to ^{238}U and $^{232}\text{Th}(\gamma,\text{f})$ cross sections (left axis).

with an about 1.2 second travel time from the irradiation end to the measurement end. During each cycle, the sample was transferred at end of bombardment (EOB), signaled by the rising edge of the final accelerator pulse. This pulse was recorded and used to reject data the HPGe recorded during irradiation. After 120 seconds of data collection, the sample holder was transferred back to the linac end and irradiation of the next cycle began. An in-hall video camera was monitored in the control room and provided a visual confirmation of the sample position for the duration of the experiments.

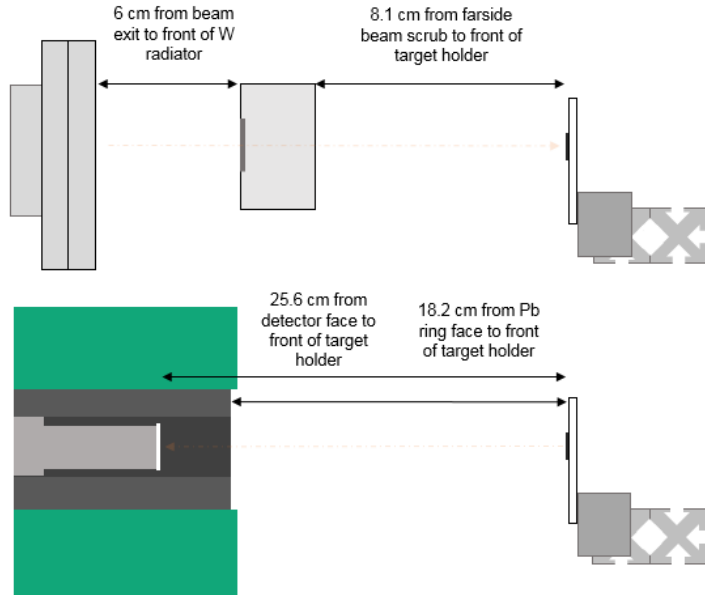


Figure 10: Diagram of sample geometry on pneumatic track at both the irradiation end (top) and the measurement end (bottom).

3.3.3 Ortec Gamma-X HPGe

A mechanically-cooled, Ortec HPGe Gamma-X was housed within the linac hall to obtain statistically significant data for the short-lived fission products. The detector was positioned at the end of the 105 cm long pneumatic transfer system to limit radiation damage to the germanium crystal.

In the linac hall, the high-voltage power source for the HPGe was kept shielded and connected to the mechanically-cooled Ortec HPGe. The output from the two detector preamplifier signals was sent to the control room where signals were amplified and shaped. The signals were connected to two separate analog-to-digital (ADC) converters: ADC1 with a range from 50 keV to about 3.5 MeV and ADC2 with an energy range from 50 keV to about 2 MeV. These two ADCs

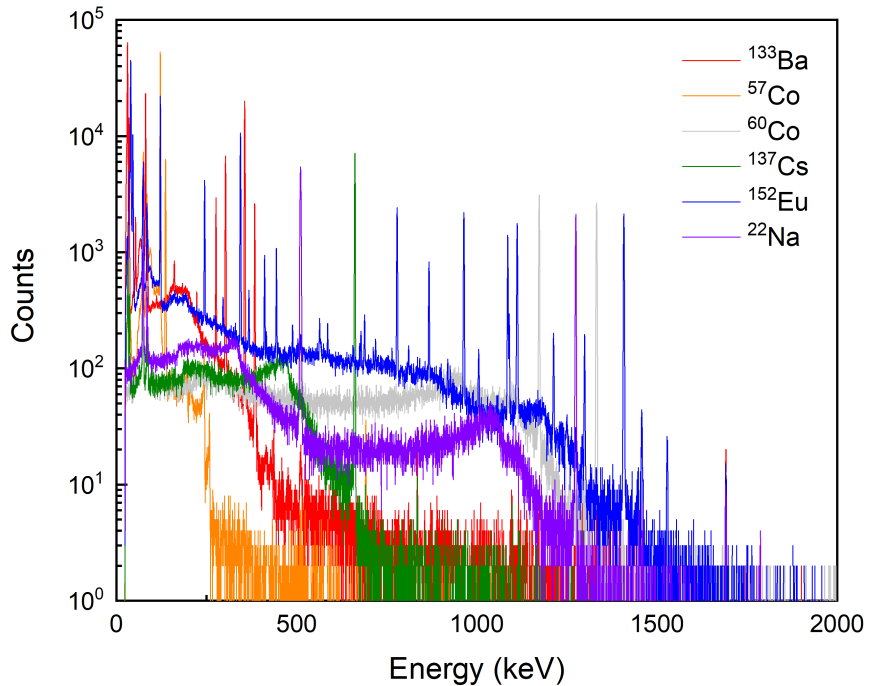


Figure 11: Measured γ -ray spectra on ADC2 used in the efficiency calibration for each sources of the in-hall HPGe detector. Energy range in efficiency calibration is from lowest energy at 53.161 keV to highest energy at 1408.006 keV.

provided inputs to the Fast ComTec multiparameter multichannel analyzer (MPA) for list-mode measurements (described further in Section 3.3.5). All of the pulse shaping electronics, ADCs, and measurement software were housed and adjusted from within the control room.

The detector energy calibration was performed using several check sources over the energy range from 79.6 keV (^{133}Ba) to 2614 keV γ -ray (^{208}Tl). The 2614 keV from ^{208}Tl was used for the energy calibrations, but not for the efficiency calibrations. The spectra of the check sources used in determining energy and efficiency calibrations for the detector are shown in Figure 11. Figure 11 illustrates the range of energies used in this work as focus for the low uncertainty fission product yield

measurements. In contrast, some previous photofission product yield measurements have focused on high-energy (>2 MeV) γ -rays for the specific application of active interrogation [39, 47].

3.3.4 Model for Detector Energy Efficiency

The efficiency calibrations of both ADC1 and ADC2 were done by modeling the efficiency using Equation (10) [48, 49], with the number of parameters, P_k determined iteratively to minimize χ^2 . The natural log of the detector efficiency is given by

$$\ln(\varepsilon) = \sum_{k=1}^m P_k (\ln(E))^{k-1}, \quad (10)$$

where m is the number of parameters in the model, P_k is the k^{th} parameter, E is the γ -ray energy, and ε is the absolute efficiency of the in-hall HPGe detector at the distance used in the experimental setup. A nonlinear fit of the calculated efficiencies for all check sources shown in Figure 11 was performed. These values for ADC1 and ADC2, as well as the final efficiency models and associated error for the in-hall detector are provided in Figure 12 and 13, respectively. The sources used to determine detector efficiency for ADC1 and ADC2 are listed in Table 6. The γ -ray energies, branching intensities, and associated uncertainty listed in Table 6 was accessed from ENSDF [50].

It is necessary to propagate the uncertainty associated with the individual variables for the efficiency model calculation. With this model, the energy efficiency of the detector at any energy will have an associated error, to be used in calculating the total uncertainty of the reported fission product yields. The sources of uncertainty considered include: the uncertainty on the activity reported for each

Table 6: γ -rays Included in HPGe Energy Efficiency Model

Check Source	γ -ray Energy (keV)	β (%)
^{137}Cs	661.657	85.1 ± 0.2
^{60}Co	1173.237	99.85 ± 0.03
	1332.501	99.9826 ± 0.0006
^{133}Ba	53.161	2.14073 ± 0.008
	80.9971	32.94855 ± 0.326
	276.398	7.16057 ± 0.049
	302.853	18.33578 ± 0.125
	356.017	62.05 ± 0.19
^{152}Eu	121.7817	10.11484 ± 0.05
	244.6975	7.5489 ± 0.041
	344.2785	26.59 ± 0.2
	411.1163	2.23702 ± 0.012
	778.904	12.92806 ± 0.083
	867.378	4.22781 ± 0.03
	964.079	14.51016 ± 0.069
	1112.074	13.66726 ± 0.069
	1408.006	20.86783 ± 0.032
^{22}Na	1274.4743	99.94 ± 0.014
^{57}Co	122.0614	85.6 ± 0.17
	136.4743	10.68 ± 0.08

calibrated check source from the manufacturer, the uncertainty in the nuclear data associated with the half-lives of the utilized nuclides, the uncertainty on the counts of each measured γ -ray peak, and the uncertainty on the nuclear data associated with the branching intensity for the γ -rays measured. An assumption was made that the energy of the individual γ -rays was not a factor in the calculated uncertainty. The uncertainty in the number counts under each measured peak is reported in the software as the deviation from a Gaussian fit. The live time of the detector measurement was also not included in the uncertainty calculation since its uncertainty was not reported in the MPANT software or output files. The MPA determines detector live time through a 1 ms clock indicating when the detector is accepting counts, so the uncertainty associated with this is likely very small with

respect to the other sources.

The equation for the calculation of partial error, ε_i , with respect to branching intensity, net counts under peak, initial activity, and half-life within the model for each individual γ -ray measurement used in the model are given by the following equations, respectively:

$$\varepsilon_\beta = \frac{\partial}{\partial \beta} \left(\frac{\frac{C}{LT}}{A_0 \cdot e^{-\lambda t} \beta} \right) \cdot \Delta \beta, \quad (11)$$

$$\varepsilon_C = \frac{\partial}{\partial C} \left(\frac{\frac{C}{LT}}{A_0 \cdot e^{-\lambda t} \beta} \right) \cdot \Delta C, \quad (12)$$

$$\varepsilon_{A_0} = \frac{\partial}{\partial A_0} \left(\frac{\frac{C}{LT}}{A_0 \cdot e^{-\lambda t} \beta} \right) \cdot \Delta A_0, \quad (13)$$

$$\varepsilon_{T_{1/2}} = \frac{\partial}{\partial T_{1/2}} \left(\frac{\frac{C}{LT}}{A_0 \cdot e^{-\lambda t} \beta} \right) \cdot \Delta T_{1/2}, \quad (14)$$

where C is the net counts under the peak for the individual γ -ray, β is the branching intensity of the measured γ -ray, $T_{1/2}$ is the half-life of the individual nuclide, A_0 is the initial activity of the check source, λ is the decay constant, and t is the time since source calibration. The errors recorded for each individual variable are given by Δ and the variable.

The method of using “micro-correlation” matrices of the determined sources of error was proposed as a simplification of error propagation in modeling HPGe detector efficiencies by Geraldo and Smith (1990) [48]. Four micro-correlation matrices were made in order to include the dependency of the error of individual variables upon one another. The micro-correlation matrices, S_β and S_C , are 21 x 21 (21 being the number of γ -ray energies used) matrices. The uncertainty on A_0

and $T_{1/2}$ for γ -ray energies originating from a single nuclide have a dependence on all other uncertainty on the γ -rays originating from the same nuclide. Six nuclides were used to determine energy efficiency, with twenty-one γ -rays in total. The micro-correlation matrices for S_{A_0} and $S_{T_{1/2}}$ are shown in (15) for the radionuclides included.

$$S_{A_0} = S_{T_{1/2}} = \begin{bmatrix} 10000000000000000000 \\ 01100000000000000000 \\ 01100000000000000000 \\ 00011111000000000000 \\ 00011111000000000000 \\ 00011111000000000000 \\ 00011111000000000000 \\ 00011111000000000000 \\ 00011111000000000000 \\ 00000000111111111000 \\ 00000000111111111000 \\ 00000000111111111000 \\ 00000000111111111000 \\ 00000000111111111000 \\ 00000000111111111000 \\ 00000000111111111000 \\ 00000000111111111000 \\ 00000000111111111000 \\ 00000000000000000100 \\ 00000000000000000011 \\ 00000000000000000011 \end{bmatrix} \quad (15)$$

The covariance matrix, $V_{\varepsilon_{i,j}}$, for all variables is calculated as the summation of the individual micro-correlation matrices, S , and partial error, ε_i , using (16).

$$V_{\varepsilon_{i,j}} = S_{\beta_{i,j}} \cdot \varepsilon_{\beta_i} \cdot \varepsilon_{\beta_j} + S_{C_{i,j}} \cdot \varepsilon_{C_i} \cdot \varepsilon_{C_j} + S_{A_{0i,j}} \cdot \varepsilon_{A_{0i}} \cdot \varepsilon_{A_{0j}} + S_{T_{1/2i,j}} \cdot \varepsilon_{T_{1/2i}} \cdot \varepsilon_{T_{1/2j}} \quad (16)$$

Solving for the parameters, P_k , of the efficiency model, the left side of Eq. 10, $\ln(\varepsilon_i)$, is set as Z_i . The covariance matrix of Z is then given by $V_{Z_{i,j}} = \frac{V_{\varepsilon_{i,j}}}{\varepsilon_i \cdot \varepsilon_j}$. With $n = 0, 1, \dots, 20$ (from the number of γ -ray efficiencies included), and $m = 0, 1, \dots, m_{max}$. The value of m_{max} was iterated to find the lowest value for χ^2 .

Both $V_{Zi,j}$ and $A_{n,m}$ (shown in Eq. (17) and Eq. (18)) are used in calculating the covariance matrix of the best fit parameters, V_P , and the vector of best fit parameters, P .

$$A_{n,m} = \ln(E_n)^m \quad (17)$$

$$V_P = (A^T \cdot V_{Zi,j} \cdot A)^{-1} \quad (18)$$

$$\hat{P} = V_P \cdot (A^T \cdot V_{Zi,j} \cdot Z_i) \quad (19)$$

Using the previously calculated values for each iterated value of m_{max} , the χ^2 value was calculated using (20). This value of χ^2 was optimized to be as close to a value of 1 as was achievable, through iterating the number of parameters. For the efficiency models of ADC1 and ADC2, the χ^2 values were 2.016 and 2.060, respectively.

$$\chi^2 = \frac{(Z - A)^T \cdot (Z - A \cdot P)}{21 - (m_{max} + 1)} \quad (20)$$

Once the 6 parameters, P_k , are found, to determine efficiency of a single energy value from the measured data, Equation (10) may be confidently used for a single energy, E , in the range of the γ -ray energies from the calibration sources used. The utility of this method is in the ability to calculate the uncertainty, or variance, σ , associated with the detection efficiency at any γ -ray energy. By using Equation (21) and (22) to solve for the covariance matrix for the calculated values, $V_{i,j}$.

$$A_C = \ln(E_i)^m \quad (21)$$

$$V_{ZC} = A_C^T \cdot V_P \cdot A_C \quad (22)$$

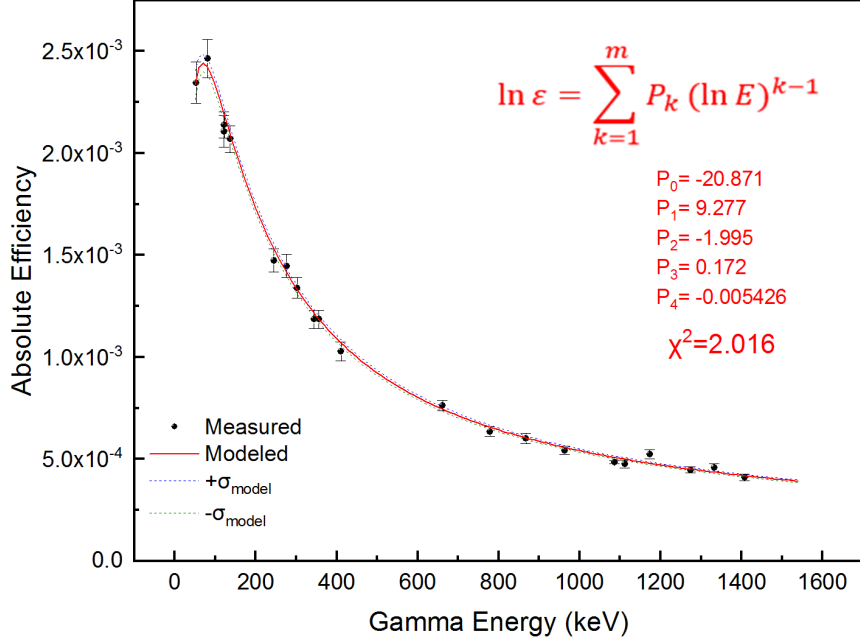


Figure 12: Ortec Gamma-X Coaxial HPGe efficiency, models (in red) and measured (in black) for ADC 1

The final variance to be used in the fission product calculation is given by (23) and (24)

$$V_{i,j} = \varepsilon_{Ci} \cdot V_{ZCi,j} \cdot \varepsilon_{Cj} \quad (23)$$

$$\sigma_{Cj} = \sqrt{V_{i,j}}. \quad (24)$$

Figure 12 and 13 report the $\pm\sigma$ of the efficiency model as dotted lines for the two detector models. By having the uncertainty incorporated in the detector efficiency model for all photon energies, the contribution to total uncertainty from the efficiency can be carried through during fission product yield calculations.

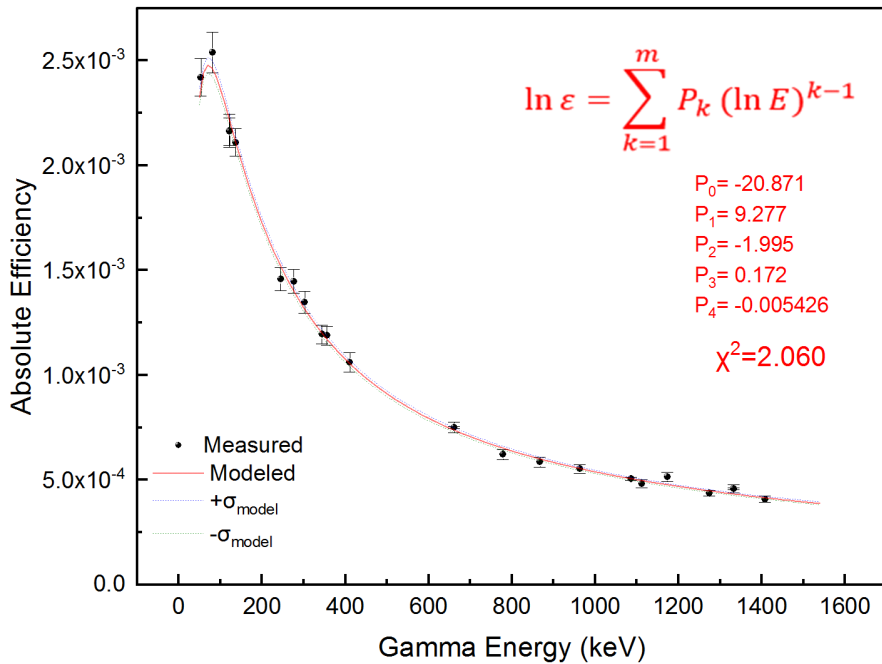


Figure 13: Ortec Gamma-X Coaxial HPGe efficiency, models (in red) and measured (in black) for ADC 2.

3.3.5 List-mode data collection

All detector data were recorded in list-mode using a Fast ComTec MPA. In list-mode, all detected counts are tagged with both energy and timing information, rather than just energy information, as may be the case in a standard multi-channel analyzer. Using the output list-file and custom parsing software specific to the project, the in-hall data were parsed into the desired range of timing bins. When analyzing the spectroscopic data, the first 2 seconds following EOB was rejected, to remove counts collected during the pneumatic shuttle travel time.

There were several approaches to parsing the data to calculate fission product yields from the in-hall cycling data. For fission products with half-lives less than

50 seconds, timing bins closest to the half-life were chosen for optimal counting statistics. The in-hall cycling data were recorded for 120 seconds of measurement time between each cycle, with a ten second buffer at the end for the sample to be moved back to the end of the linac. This 120 second cycling count scheme was optimized for those short-lived fission products. For fission products with half-lives longer than 50 seconds, the sample was instead transferred to the auxiliary counting detection setup for extended counting after an irradiation was primarily used to calculate those with half-lives longer than 50 seconds.

3.4 Fission Product Yield Analysis

3.4.1 Fission Product Yield Using Single Timing Bin

To calculate the yield of an individual nuclide, the total number of atoms for the measured nuclide at EOB is required. Knowing the net counts under an individual γ -ray peak (C), the number of emissions from the nuclide of interest is calculated through an adjustment using the branching intensity (β), the transmission of that γ energy in the material (A_p), the absolute detector efficiency at that energy (ε), and the ratio of the real-time to the live-time of the detector measurement (dead-time correction). Transmission, A_p , is calculated using Equation 6 for a particular target.

During a constant irradiation, the number of emissions in the timing bin is calculated by integrating the activity decay rate equation from the start of counting, t_s , to the end of the measurement, t_f , both relative to EOB, as shown by Equation 25. Separating the initial number of atoms of interest, $N(0)$, and the decay constant, λ , from activity $A(t)$, the relationship can be rearranged to solve for $N(0)$, as shown by Equation 26.

$$\frac{C}{\beta\varepsilon A_p} \cdot \frac{RT}{LT} = \int_{t_s}^{t_f} A(t)dt = \int_{t_s}^{t_f} \lambda_i N(0) \cdot e^{-\lambda t} dt \quad (25)$$

$$N(0) = \frac{\frac{C}{\beta\varepsilon A_p} \cdot \frac{RT}{LT}}{(e^{-\lambda t_s} - e^{-\lambda t_f})} \quad (26)$$

Irradiation during the in-hall photofission experiments can not be assumed to be constant because the linac operates in pulse mode. A rapid cycle of production and decay of the short-lived fission products of interest occurs during the experiment; the number of cycles and individual linac pulses must be included due to the decay of products occurring both between linac pulses and during the measurement only portion of the cycle. The number of individual linac pulses during irradiation is determined by multiplying the repetition rate, $1/\tau$ (Hz), by the irradiation time. Each linac pulse event was also measured with a signal and recorded in ADC3. This signal was used in the parsing process to determine EOB. The experimental values for C_{cycles} and $1/\tau$ are listed in Table 5. The denominator of Equation (27) is an adjustment of Equation (26), specific to the cycling and pulsing structure used in the experimental setup. The calculation of $N(0)_{pp}$ with respect to the cycling and pulsing to achieve optimal statistics is given by

$$N(0)_{pp} = \frac{\frac{C}{\beta\varepsilon A_p} \cdot \frac{RT}{LT}}{\sum_{M=0}^{cycles-1} \sum_{m=0}^{pulses-1} \int_{t_1}^{t_2} \sum_{i=0}^M e^{-\lambda[(T_M - T_i) + t + (m \cdot \tau)]} \lambda dt}, \quad (27)$$

where t_1 and t_2 are the start and end of the parsed timing bin that measurements are taken with respect to the end of each cycle. T is the time the i^{th} cycle starts, relative to the start of the first cycle. So, the variable T_M refers to the summation of total irradiation time from start of irradiation to the end of cycle, M , while T_i is used to call the total time since start of irradiation of each subsequent cycle.

This method solves for the number of atoms of a specific fission product produced per linac pulse, the fission product yield is then calculated as a ratio of individual product yield per pulse over total photofission events per pulse, $Y_{fissions,pp}$:

$$Y_{FPi} = \frac{N(0)_{pp}}{Y_{fissions,pp}}. \quad (28)$$

This method is most useful with short-lived fission products for which the measured data were best available in one large time bin, optimized for counting statistics and deconvolution of the peaks. If the half-life of the nuclide of interest was on the order of the size of a single time bin, it is possible there would not be sufficient counting statistics to calculate fission product yields using the integral solver method described in the next section.

3.4.2 Fission Product Yield Using an Integral Solver

The list-mode data collected provides additional flexibility and information in analyzing nuclides of interest, especially those with very short half-lives, as they build in and quickly decay. For all the in-hall cycling data, the measurements were parsed to eliminate the first 2 seconds of measurement following EOB. This eliminates data recorded during the pneumatic transfer of the sample, with some buffer time to ensure proper sample placement in front of the HPGe detector. After the first two seconds, the width of time bins, Δb , was chosen to be roughly half of the half-life of the nuclide to optimize counting statistics within each individual time bin. For example, ^{99}Zr has a half-life of 2.1 seconds, so timing bins with a 1 second interval were chosen to balance the counting statistics within the individual bins and number of bins contributing to the analysis.

After the list-mode data was parsed into time bins, the net peak area for the

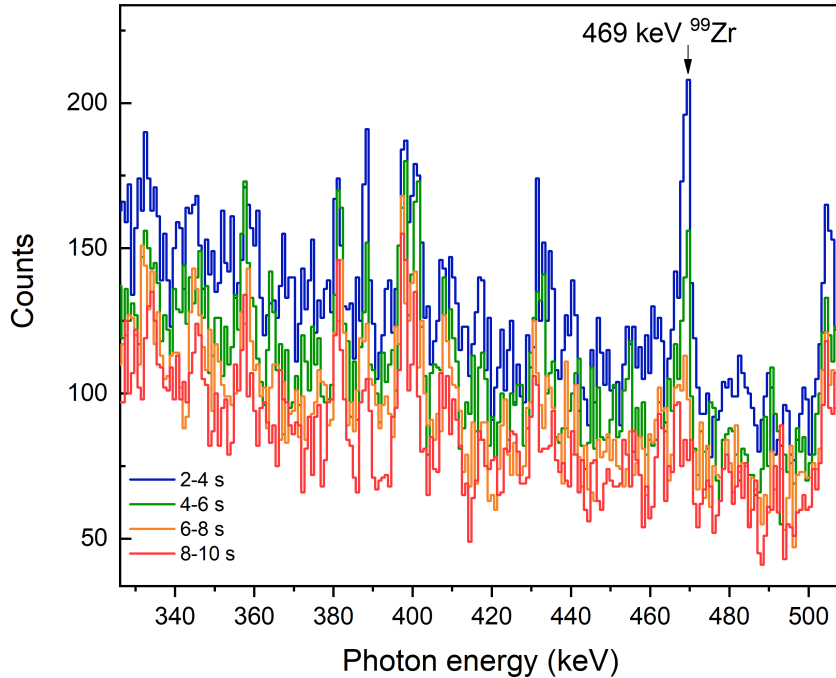


Figure 14: ^{238}U irradiated at $B=8$ MeV list-mode data parsed into 2 s interval bins to visualize the decay of ^{99}Zr by its 469 keV peak.

γ -ray of interest, C , for each timing bin was determined. The number of counts under a peak along with the error associated with the peak fit were determined and set with respect to x , the mid-point of the bin. Peak analysis was performed using OriginPro 2018. In this process the convolution (the overlapping of multiple γ -rays when an energy peak was not Gaussian) was considered and included in much of the analysis.

An integral fit was performed over the timing bins to calculate the yield of the nuclide of interest and those considered in its decay chain. The decays of parent nuclides into the nuclide of interest are included by using radioactive decay rate equations that solve for the activity of a first, second, or third order decay chain.

The solution of an integral fit of this equation across each time bin (from $x - \frac{\Delta b}{2}$ to $x + \frac{\Delta b}{2}$) obtains the parameters of interest. This process simultaneously solves for the number of atoms at EOB, $N(0)$, for the nuclide(s) of interest, as well as uses the decay constants, λ , of the nuclides involved within the decay chain as a fit parameter. When performed correctly, the decay constants in the solution of the integral fit should closely match the known values for each nuclide. If not, there could be additional γ -rays being counted in that bin from another source of the same or close γ -ray energy. The basic form of the integral solver is given by

$$R_i = \int_{x-\frac{\Delta b}{2}}^{x+\frac{\Delta b}{2}} A(t) dt \quad (29)$$

where $A(t)$ is the activity equation for the atoms of the nuclide of interest and $x \pm \frac{\Delta b}{2}$ is the beginning or the end of each timing bin (using the mid-point time, x , to calculate). The parameters within the activity equation $N(0)_i$ and λ_i are required for the final fission product yield.

As in the other method, the number of fission products produced per linac pulse, $N(0)_{pp}$, the fission product yield is calculated using the experimental setup adjusted seen in Equation (27), as a ratio of atoms of the specific fission product per pulse over total photofission events per pulse, $Y_{fissions,pp}$. This method was most useful with very short-lived fission products that fully decay by the end of the cycle.

3.5 Calculation of Photofission Events From ^{237}U Production

The fission events per pulse, $Y_{fissions,pp}$, is required in the calculation of absolute fission product yields. Rather than total fissions for the irradiation, the photofission reaction yield per linac pulse, $Y_{fissions,pp}$, was used to maintain consistent

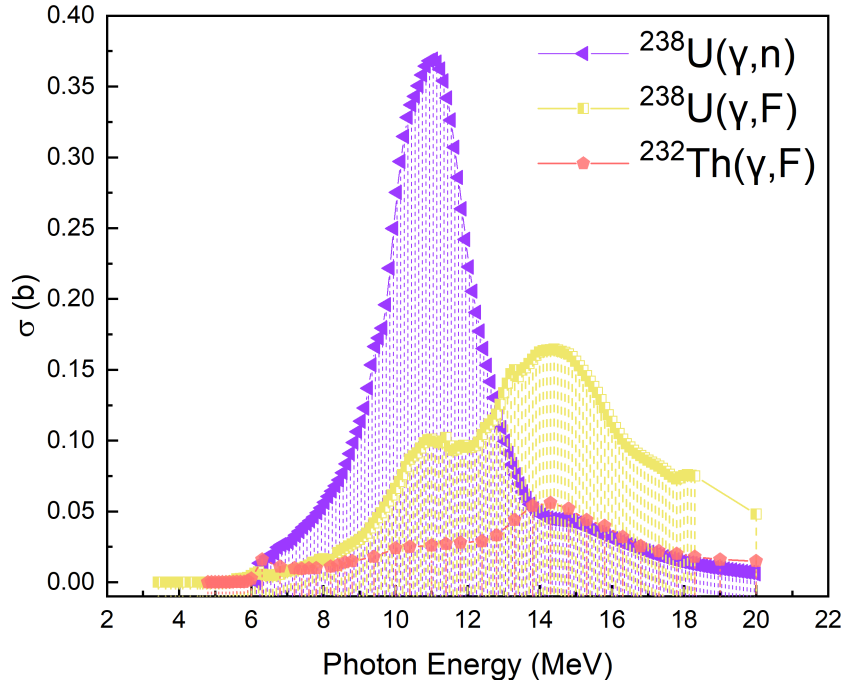


Figure 15: $^{238}\text{U}(\gamma, n)$, $^{238}\text{U}(\gamma, f)$, and $^{232}\text{Th}(\gamma, f)$ cross sections used in calculating photofission events per pulse.

calculations among all six experiments (2 targets, 3 energies).

Figure 15 provides a visual comparison of the $^{238}\text{U}(\gamma, f)$ reaction (in yellow) with the $^{238}\text{U}(\gamma, n)$ (in purple). It can be seen that at relatively lower energies, 6 to 14 MeV, the production of ^{237}U is expected to be significant with respect to photofission production. The $^{238}\text{U}(\gamma, n)$ reaction produces ^{237}U , the decay of which is accompanied by the emission of a γ -ray at 208.0 keV ($\beta = 21.2\%$) that could be measured in experimental spectroscopic measurements.

First the number of ^{237}U atoms at EOB, $N_{237,0}$, must be calculated using the same method as described with Equation (26). The uncertainty for the number of atoms of ^{237}U was calculated considering the uncertainty on the number of counts

under the 208.0 keV peak, uncertainty in the detector efficiency model at 208.0 keV, the branching intensity, β , of 208.0 keV for ^{237}U decay, the attenuation of the 208.0 keV γ -ray in the uranium sample, and the uncertainty of the decay constant for ^{237}U from ENSDF [50].

The number of ^{237}U at EOB includes the periods of irradiation and decay during the pulsing of the linac. Calculating the ^{237}U yield per pulse requires knowledge of the linac period (reciprocal of repetition rate), τ , and the number of pulses in an individual irradiation cycle, p . The yield per linac pulse of ^{237}U , $Y_{237,pp}$ is given in Equation 30.

$$Y_{237,pp} = \frac{N_{237,0}}{\sum_{M=0}^{\text{cycles}-1} \sum_{m=0}^{\text{pulses}-1} \int_{t_1}^{t_2} \sum_{i=0}^M e^{-\lambda[(T_M - T_i) + t + (m \cdot \tau)]} \lambda dt} \quad (30)$$

The ratio of the number of photofission events to ^{237}U production is proportional to the ratio of the $^{238}\text{U}(\gamma, f)$ to $^{238}\text{U}(\gamma, n)^{237}\text{U}$ cross sections, when using the same incident bremsstrahlung X-ray spectrum. Using this logic and the bremsstrahlung X-ray spectrum incident on target, the number of photofission events per pulse was calculated. The calculation of number of photofission events per pulse, $Y_{U238,fissions,pp}$, is given by

$$Y_{U238,fissions,pp} = Y_{237,pp} \cdot \frac{\int_0^B \frac{dC(B,E)}{dE} \sigma_{U238\gamma,f}(E) dE}{\int_0^B \frac{dC(B,E)}{dE} \sigma_{U238\gamma,n}(E) dE}, \quad (31)$$

where B is the endpoint energy, E is the incident photon energy, $\sigma_{U238\gamma,f}(E)$ is the photofission cross section, $\sigma_{U238\gamma,n}(E)$ is the ^{237}U production cross section, and $C(B, E)$ is the number of photons in the bremsstrahlung photon spectrum. The bremsstrahlung spectrum per pulse, $C(B, E)$ is determined using an MCNP6

model. Such simulations were validated using the experimental measurements and are described in the following chapter in more detail.

^{231}Th has no high-intensity delayed γ -rays that could be reliably measured in the experimental spectroscopic measurements. Although preferred, the number of fissions was not determined experimentally based on measurement of $^{232}\text{Th}(\gamma,\text{n})$ production. Rather, a ratio of the $^{238}\text{U}(\gamma,f)$ and $^{232}\text{Th}(\gamma,f)$ cross sections was used to adjust the experimentally calculated number of fissions per pulse for ^{238}U , $Y_{\text{U}238,\text{fissions},\text{pp}}$, to the number of fissions per pulse for ^{232}Th , $Y_{\text{Th}232,\text{fissions},\text{pp}}$. Solving for the ^{232}Th photofission production per pulse, $Y_{\text{Th}232,\text{fissions},\text{pp}}$, using the ratio of the ^{238}U and ^{232}Th photofission cross sections, $\sigma_{\text{U}238\gamma,f}(E)$ and $\sigma_{\text{Th}232\gamma,f}(E)$, is given by

$$Y_{\text{Th}232,\text{fissions},\text{pp}} = Y_{\text{U}238,\text{fissions},\text{pp}} \cdot \frac{\int_0^B \frac{dC(B,E)}{dE} \sigma_{\text{Th}232\gamma,f}(E) dE}{\int_0^B \frac{dC(B,E)}{dE} \sigma_{\text{U}238\gamma,f}(E) dE}. \quad (32)$$

The uncertainty contribution from an offset of the target from the bremsstrahlung X-ray beam in the calculation of fission yield is described in Section 4.3. The final calculated fission events per pulse with uncertainty is given in Section 4.4.

4 Characterization and Simulation

4.1 Introduction

MCNP6 simulations were performed at several points in the experimental setup to supplement the data collected in the experimental measurements and obtain further insight necessary for the calculation of the short-lived fission product yields. The geometry of both the irradiation and measurement ends of the experimental setup were modeled with high geometric and material fidelity in MCNP6. The irradiation end model and simulations were used to characterize the bremsstrahlung X-ray flux, the number of photofissions for each irradiation, as well as the contributions of uncertainty in the calculated number of photofissions per pulse. The simulations on the measurement end aided in collecting example γ -ray spectra from the modeled HPGe to verify the fission product yield analysis method. This section includes descriptions of the MCNP6 simulations focused on obtaining further information at both ends of the experiment, in-hall irradiation and in-hall measurement.

4.2 Bremsstrahlung X-ray Flux on Target

An MCNP6 model of the irradiation end was created using the geometry and materials of the linac and irradiation end of the experimental setup. For each pair of electron beam endpoint energy and target material, simulations were run to characterize the bremsstrahlung X-ray spectrum. Details of the current monitor, tungsten radiator, aluminum beam scrub, sample holder, and beam exit were used in the model of the output linac electron beam to characterize the flux on target. To inform the MCNP6 source energy distribution for the electron beam, experimentally measured energy distributions of the electron beams at endpoint energies

of 8, 14, and 20 MeV were used. These beam energy distributions were measured by bending the electron beam at discrete energies, using a magnetic field, to the 90 degrees position. These bent fractions of the total electron beam at a specific energy were then measured using a Faraday cup. Discrete energies above and below the expected endpoint energy were stepped through and the total charge was measured for each energy.

The result of the experimentally measured energy distribution of the electron beams is seen in Figure 16. The yellow points are the experimentally measured charges at several discrete energies. The red dotted line is an interpolation of the experimentally measured data points using an Akima spline, producing a 200 point fit. These interpolated beam energy distributions were used to reproduce the electron beam for the source definition (SDEF) in MCNP6. The discrete energy values were modeled as the energy of the particle sampled from the electron source, with the associated probability of each discrete energy being weighted by the integrated charge per pulse. As the number of electrons can be inherently determined using the charge per pulse measured, this value was used as a surrogate for the probability of each discrete energy.

This method was a more accurate representation of the actual electron beam energy distribution when compared to simply modeling the electron beam energy as a monoenergetic source using the endpoint energy, as it had been done earlier in the project. The charge distribution method was compared to modeling the electron beam as a monoenergetic source by comparing the photon flux on target from an F4 tally in MCNP6. This F4 tally of the resulting bremsstrahlung X-ray spectrum was then used to calculate average excitation energy, $\langle E^*(B) \rangle$. The result of this comparison showed that to produce a comparable average excitation energy

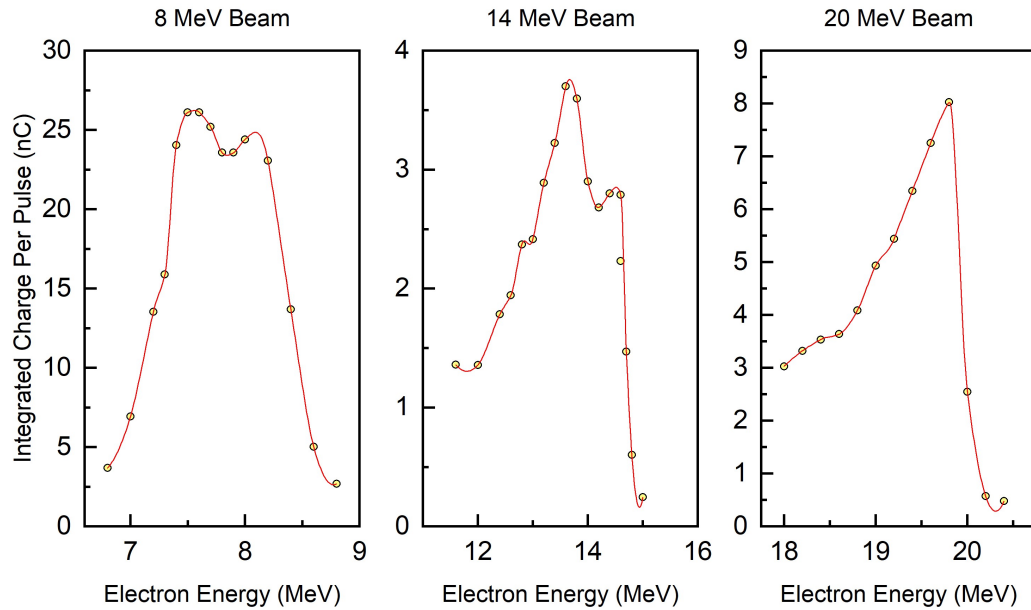


Figure 16: Measured energy distribution of the $B=8$, 14, and 20 MeV electron beams.

using a monoenergetic source for the electron beam, the monoenergetic electron energy in MCNP6 would need to be significantly lower than the endpoint energy. For example, using a beam energy of about 19.15 MeV was required to match the average excitation energy of the target ^{238}U nucleus calculated using the beam charge distribution method of the $B=20$ MeV beam.

4.2.1 Calculation of Photofission Yield Per Pulse Using Simulation

The experimentally measured photofissions per pulse for ^{238}U (described in Section 3.5) were used as the reference in adjusting the linac-end MCNP6 model to match that of ^{238}U in the number of fissions produced using (33) and (34). Equation (33) was used to calculate the photofission events per pulse, ς , using the simulation-produced bremsstrahlung X-ray energy spectrum, $C(B, E)$.

$$\varsigma = N_T \int_0^B \frac{C(B, E)}{\Delta E_{step}} \cdot \sigma_{\gamma,f}(E) dE \quad (33)$$

The difference in the discrete energies output in the MCNP6 F4 tally for the bremsstrahlung X-ray flux is ΔE_{step} . Figure 17 shows the final bremsstrahlung X-ray flux, $C(B, E)$, modeled using the charge distribution for $B=8, 14$, and 20 MeV. Vertical droplines better illustrate the energy range on the X-axis that each of the three beams cover. Photofission events per pulse, $Y_{emp,pp}$, are calculated using the average charge, $Q_{Average}$. This adjustment is given in (34).

$$Y_{sim,pp} = \varsigma \cdot \frac{Q_{Average}}{1.602189 \cdot 10^{-10} \text{ nC}} \quad (34)$$

The experimentally measured value for $Q_{Average}$ for each experiment is listed in Table 5. The average number of electrons per linac pulse is calculated by dividing by the elementary charge, $1.602189 \cdot 10^{-10}$ nC, normalizing ς by the average number of incident electrons per pulse from the linac. This determines $Y_{sim,pp}$, the number of photofission events per pulse. This step is required because the photon fluence determined through MCNP6 simulations needs to be normalized by the number of source electrons.

4.2.2 YZ Mesh Tally of Photon Beam on Target

Using the irradiation end model, a characterization of the electron beam shape on target was performed. During the week of experiments, glass slides were briefly irradiated at the exact position of the sample holding position. These were used to set the laser in alignment and ensure the beam was centered on the target foils. Figure 18 is a scan of these glass slides with the discoloration of the glass due to the incident electron beam. Using the laser to align samples for irradiation also

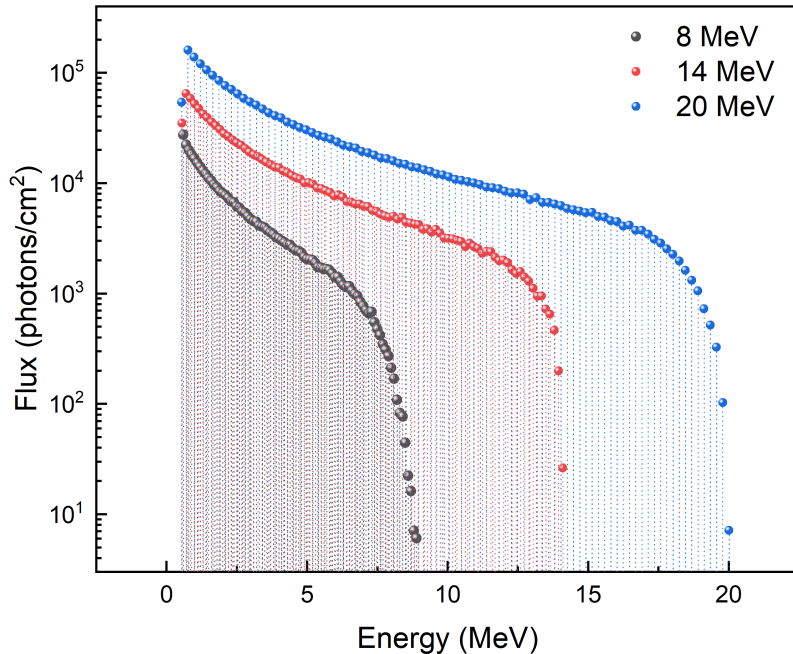


Figure 17: MCNP6 produced bremsstrahlung X-ray spectra incident on target with endpoint energies 8, 14, and 20 MeV.

allowed for better reproducibility across the experiments.

A set of MCNP6 simulations was performed to produce mesh tallies of photons and electrons in a 2 cm^2 area on the YZ-plane at the target position (the Z-plane being parallel to the foil and the Y-plane along the trajectory of the pneumatic transfer system). These mesh tallies mapped the intensity of the electron and photon beams with respect to YZ-position that was incident on the thorium and uranium foil samples. Figure 19 shows the photon (top) and electron (bottom) tallies for the 8, 14, and 20 MeV endpoint energy beams. The source was defined as a 3 mm diameter disk source of electrons within the vacuum, just inside the expected output of the linac. Scattering of the electrons as they travel through

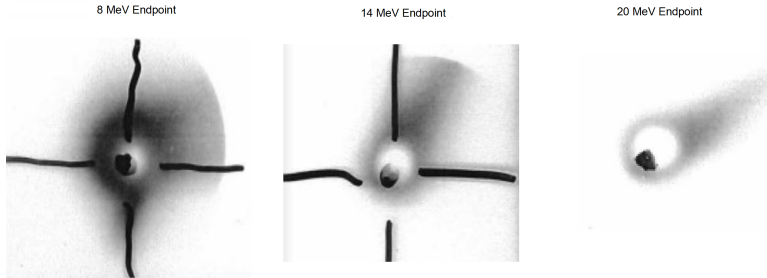


Figure 18: Transparent glass slides discolored by the electron beam at the sample position for endpoint energies $B=8$, 14, and 20 MeV.

air to the radiator influences the beam spread to some degree. The uranium foil from the simulation can be seen in the electron mesh tallies due to the photon interactions occurring within the sample. Good agreement was found between the shape of the beam as shown by the glass scans and the 2D YZ-plane mesh tallies.

4.2.3 3D Mesh Tally of Bremsstrahlung X-Ray Production

Several simulations using MCNP6 were used to produce 3D mesh tallies for both electrons and photons at all three of the endpoint energies. This was performed as a way to visualize how the electron beam interacts with the tungsten converter and aluminum beam scrub to result in the bremsstrahlung X-ray beam incident on target. A 3D mesh from the point of exit for the electron beam to 0.5 cm past the sample position was performed. These mesh tallies were run for electrons and photons for each respective endpoint energy.

The top row of Figure 20 shows the output electron beam from the linac in 3D. The interaction with the tungsten radiator can be seen (the thin, rectangular foil inset at the near-linac end of the grey component). The spread of the electron beam upon interacting with the tungsten can also be seen. The opacity of the beam was set to the same log-scale for the three energies for comparison of the intensity

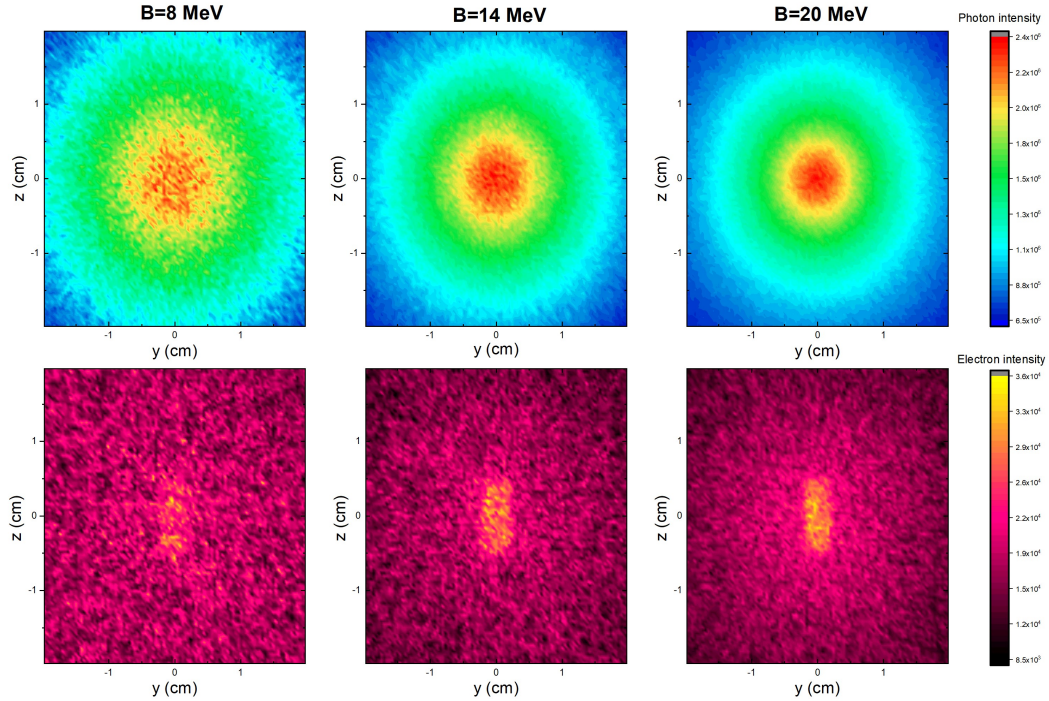


Figure 19: MCNP6-produced intensity distributions of the bremsstrahlung X-ray beam (top) and electrons (bottom) at sample position at $B=8$, 14, and 20 MeV.

and shape of the three electron beams. The penetration depth of the beam into the radiator and scrub components can be seen to increase with increasing endpoint energy.

The bottom row of Figure 20 shows both the electron beam and resulting photon beam. The difference in the intensity and shape of the bremsstrahlung X-ray spectrum is shown with respect to the incident electron beam energy. The higher electron beam energy has a higher conversion efficiency for bremsstrahlung X-rays and the “tightness” of the photon beam at the exit of the aluminum beam scrub is also reflected in Figure 19. As opposed to the electron scale, the three photon beams seen in Figure 20 have different scales due to their large difference

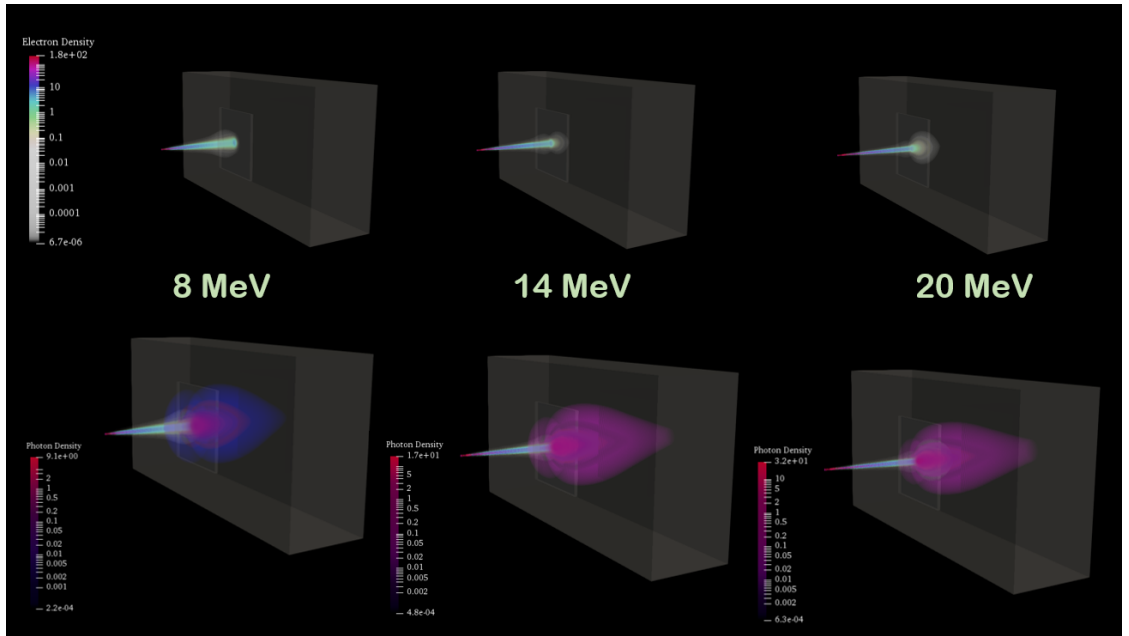


Figure 20: 3D visualization of the electron and bremsstrahlung X-ray beams for 8, 14, and 20 MeV endpoint energies produced with MCNP6 simulation.

(increasing number of photons with increasing incident energy). The opacity and color scale was chosen among the three to still allow for comparison of the shape of the respective photon beams, independent of increasing intensity.

4.3 Uncertainty Considerations on the Photofission Yield Per Pulse

4.3.1 Target Offset from Beam

Even a minor offset of a small target could result in a significant difference in the number of photofission events per pulse with respect to the center position. This difference in the number of fissions in a foil with an offset was characterized through 121 simulations incrementally moving the target foil down and to the left to a maximum of 0.5 cm for each pair of experimental setup. Since the number of photofissions per pulse for ^{238}U was calculated by using the ratio of $^{238}\text{U}(\gamma, f)$ to

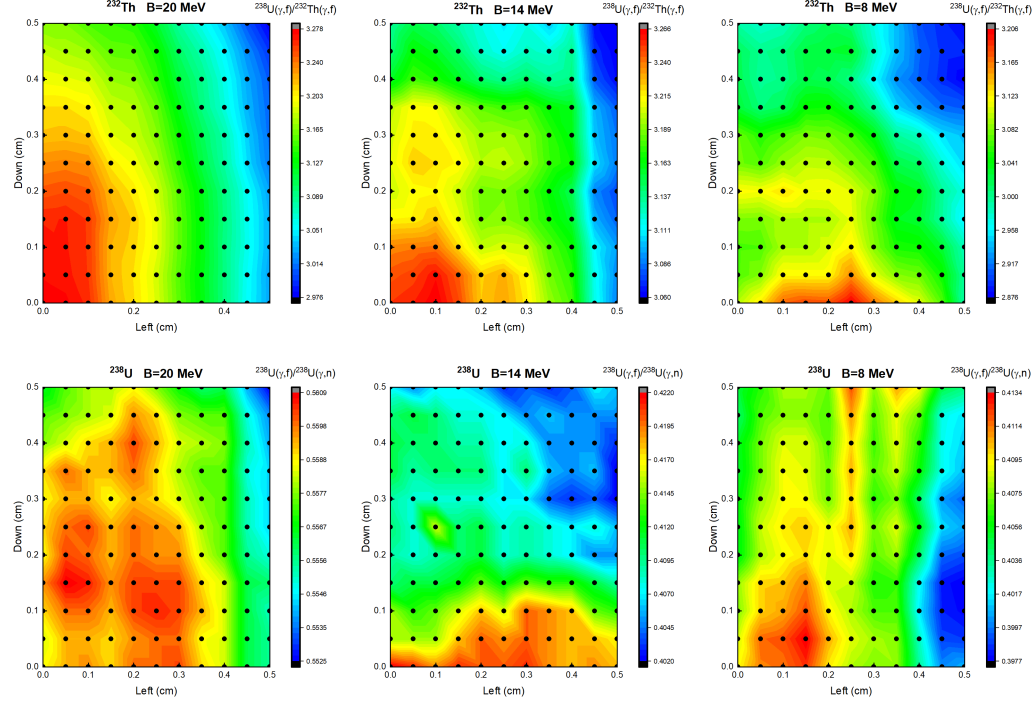


Figure 21: (Top) Ratio of $^{238}\text{U}(\gamma, f)$ and $^{232}\text{Th}(\gamma, f)$ yields with respect to offset from center to the left and down in thorium foil, (Bottom) Ratio of the $^{238}\text{U}(\gamma, f)$ and $^{238}\text{U}(\gamma, n)$ yields for offset from center to the left and down in uranium foil.

$^{238}\text{U}(\gamma, n)$ cross sections, this cross section ratio was calculated using the incident photon spectrum at each position from the 121 offset simulations per target. The mean value and standard deviation of the 121 calculated ratios were calculated and used in the experimental calculation of photofissions per pulse from ^{237}U , so it included the uncertainty contribution of a potential offset of the target. Symmetry of the beam was assumed so the simulated quarter slice represents an offset in any YZ direction.

The photofissions per pulse of ^{232}Th was not calculated using measurement of ^{231}Th so the ratio of $^{232}\text{Th}(\gamma, f)$ to $^{232}\text{Th}(\gamma, n)$ was not used, rather the ratio of $^{238}\text{U}(\gamma, f)$ to $^{232}\text{Th}(\gamma, f)$ was used. The ^{238}U and ^{232}Th photofissions per pulse and

uncertainty are reported in Table 7.

Figure 21 illustrates how the scale of differences in the cross section ratios per pulse differs for each electron beam endpoint energy. The 20 MeV and 14 MeV show an increasing number in the percent difference in fissions with increasing offset, highlighting how the “tightness” of the photon beam with higher energies affects the flexibility of target position.

4.3.2 Neutron Fission in Target

The neutron energy distribution within the foil during irradiation was necessary to ascertain if the contribution of neutron fissions would be a significant source of uncertainty in the calculated number of photofission events per pulse. For each pair of electron endpoint beam energy and target, an MCNP6 simulation was performed to obtain the photon energy distribution directly at the face of the target. A second set of MCNP6 simulations used the result as a photon source in the direction of the beam to produce the neutron energy distribution within the target foils. This was done to ensure acceptable statistics in the simulation. Figure 22 compares the neutron energy distribution for each electron beam endpoint energy in units of neutrons per source photon (on the left Y axis) with respect to the neutron fission cross section for both targets (on the right Y axis). Thorium and uranium neutron fission cross sections are from ENDF/B-VIII.0.

The neutron energy distributions were used to calculate the number of neutron fissions per pulse in each target. Since the neutron energy distribution is in units of neutrons per source photon, the number of photons per pulse was calculated using the average charge per pulse and the fraction of photons per source electron. The neutron energy distribution, the number of photons per pulse, and the neutron

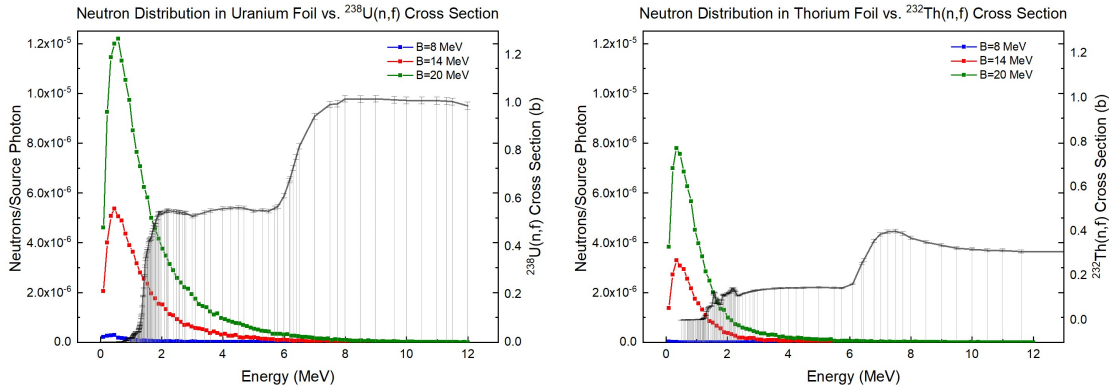


Figure 22: Neutron energy distribution in Both Foils for $B=8$, 14 , and 20 MeV with respect to neutron fission cross section.

fission cross section were needed to solve for the final number of neutron fissions per pulse.

The percent of the total calculated fissions per pulse from neutron fissions of ^{238}U was negligible for all three endpoint energies. As a percent of the total calculated fissions, these were 0.01% for 8 MeV, 0.18% for 14 MeV, and 0.24% for 20 MeV. Since the total uncertainty on the ^{238}U fissions per pulse was 2.6%, 2.8%, and 5.0% for 8, 14, and 20 MeV, respectively, the neutron fissions from ^{238}U are well within the uncertainty on the photofissions per pulse. Similarly, the neutron fission within the target of ^{232}Th resulted in 0.09% for 20 MeV, 0.03% for 14 MeV, and $10^{-6}\%$ for 8 MeV of the total calculated fission events per pulse.

4.3.3 Fission of Impurity Actinides

The uncertainty contribution in the number of calculated fissions from the photofission of ^{235}U in the uranium foil was determined to be negligible. The atom percent of ^{235}U in the target was determined to be 0.736% through ICP-MS. The calculated percent of photofissions per pulse from ^{235}U was $3.1 \cdot 10^{-4}\%$ for the 20

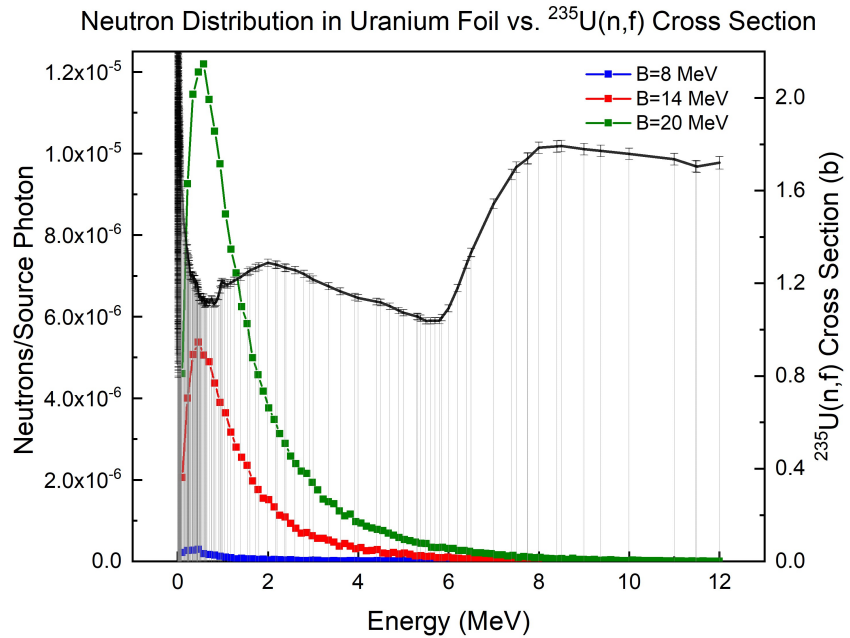


Figure 23: Neutron energy distribution in Uranium foil for $B=8$, 14, and 20 MeV with respect to ^{235}U neutron fission cross section.

MeV irradiation. When compared to the uncertainty of 5.0% on the fissions per pulse calculation for 20 MeV, the fission of ^{235}U in the foil is statistically insignificant. Similarly, the percent of photofissions per pulse from ^{235}U was $1.4 \cdot 10^{-3}\%$ and $2.1 \cdot 10^{-3}\%$ for the 14 MeV and 8 MeV irradiations, respectively. These contributions are statistically insignificant when compared to the uncertainty of 2.8% for 14 MeV and 5.0% for 8 MeV on the total fissions per pulse.

The contribution from neutron fissions per pulse from ^{235}U was more than that from photofission of ^{235}U , but still statistically insignificant when compared to the total uncertainty in the calculated photofissions per pulse. Figure 23 shows the neutron energy distribution within the uranium foil with respect to the $^{235}\text{U}(n,f)$ cross section (cross section data from ENDF/B-VIII.0). For 8, 14, and 20 MeV, the neutron fission contributions as a percent of total calculated photofissions per

pulse were $2.1 \cdot 10^{-3}\%$, $3.9 \cdot 10^{-3}\%$, and $4.5 \cdot 10^{-3}\%$, respectively.

The thorium target foil was confirmed with the ICP-MS analysis (Table 3) to be $99.99992 \pm 0.00002\%$ ^{232}Th . The fission contribution of trace ^{228}Th , ^{229}Th or ^{230}Th would be virtually zero and was not included in the uncertainty calculation of ^{232}Th fissions.

4.4 Fission Events Per Linac Pulse

Table 7: Photofission Events Per Pulse

Target	B (MeV)	$\langle E^*(B) \rangle$ (MeV)	Fission Events Per Pulse
^{238}U	8	6.78 ± 0.01	493 ± 13
^{238}U	14	10.30 ± 0.01	$11,980 \pm 330$
^{238}U	20	12.59 ± 0.01	$123,700 \pm 6,300$
^{232}Th	8	6.74 ± 0.02	374 ± 10
^{232}Th	14	9.22 ± 0.01	4950 ± 160
^{232}Th	20	11.50 ± 0.03	$40,000 \pm 1,600$

The uncertainty on the calculated number of ^{238}U and ^{232}Th photofissions per pulse includes the uncertainty on the peak area of the 208.0 keV peak, the branching intensity, the uranium foil thickness, ratio of photonuclear cross sections, and the detector efficiency. This was propagated through each calculation from the initial number of ^{237}U through the final number of fissions per pulse.

4.5 Modeling of HPGe Detector Response in MCNP6

To visualize any discrepancies in the photonuclear data utilized by computational tools, as well as an indication of what γ -rays contributed to peaks seen in the experimental measurement, a high-fidelity MCNP6 model of the in-hall HPGe detector was used to simulate the spectroscopic detector response. The geometry of the crystal and housing specific to the Ortec Gamma-X Coaxial HPGe used in

the experiments were used to model the detector in MCNP6. This HPGe detector model was placed in the configuration used in experimental setup, considering the surrounding shielding and the pneumatic track.

Producing a comparable γ -ray spectra, an F8 tally for photons and electrons incident on the active volume of the detector was used. The Gaussian Energy Broadening (GEB) card was used to best reflect the energy resolution. The GEB card in MCNP6 models the full width at half-maximum (FWHM) of a γ -ray peak as a function of energy, given by

$$FWHM = A + B \cdot \sqrt{E + C(E^2)} \quad (35)$$

where E is the γ -ray energy in MeV, $FWHM$ is the resolution of the γ -ray peak in MeV, and A , B , and C are constants used in the GEB card. The same sources used in the efficiency calibration of the Ortec HPGe detector at the sample position were used to determine the value of A , B , and C . The resolution of the detector as a function of γ -energy is given in Figure 24. After plotting the resolution of the γ -rays from ^{137}Cs , ^{60}Co , ^{133}Ba , ^{152}Eu , ^{22}Na , and ^{57}Co , a non-linear least squares fit using Equation (35) was performed to find the constants for ADC1 and ADC2.

MCNP6 models of check sources of ^{137}Cs , ^{60}Co , ^{133}Ba , and ^{152}Eu at the measurement end of the setup were performed to match the total the number of expected X-ray and γ -ray emissions during the time interval from the in-hall γ -ray measurements for these four sources. The simulated sources were used to compare the MCNP6 simulated F8 tally-produced γ -ray spectra to those that were measured for the efficiency calibration. The desire was to match both the energy efficiency and area under the peak the comparable γ -rays. The goal was to get the net peak area for the γ -ray peaks in the spectra to match within 5% difference. Among

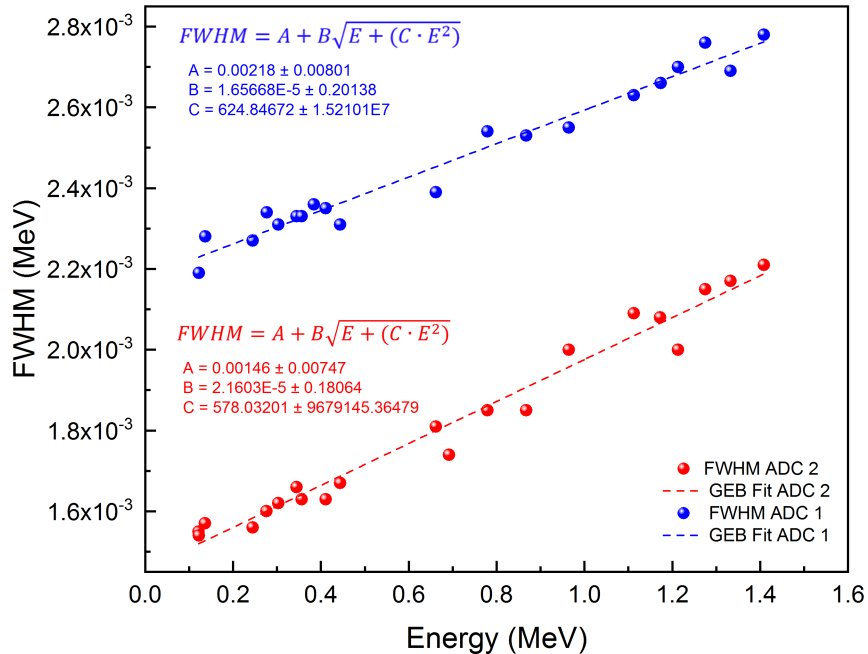


Figure 24: FWHM vs. photon energy to determine input values for the MCNP6 Gaussian Energy Broadening (GEB) card.

the four nuclides, the γ -rays analyzed were 122 keV, 244.9 keV, 276 keV, 303 keV, 344.56 keV, 356.29 keV, 444.28 keV, 662 keV, 867 keV, 964.5 keV, 1112.7 keV, 1173 keV, and 1332 keV. Of the γ -ray peaks analyzed, only the 122 keV (7.4% difference) and 244 keV (5.8% difference) had a net peak area difference greater than 5%. The average difference in net peak area for the listed γ -rays being 4.1%.

Figure 25 is the comparison of the γ -ray spectra for ^{137}Cs , ^{60}Co , ^{133}Ba , and ^{152}Eu of the simulated γ -ray spectra (in black) with respect to the measured γ -ray spectra (in red) for ADC2. The measured and simulated spectra for ^{137}Cs , ^{60}Co , and ^{152}Eu all visually match well at the high peaks, but there is some visual discrepancy between simulated and measured in the ^{133}Ba . Figure 26 shows how the

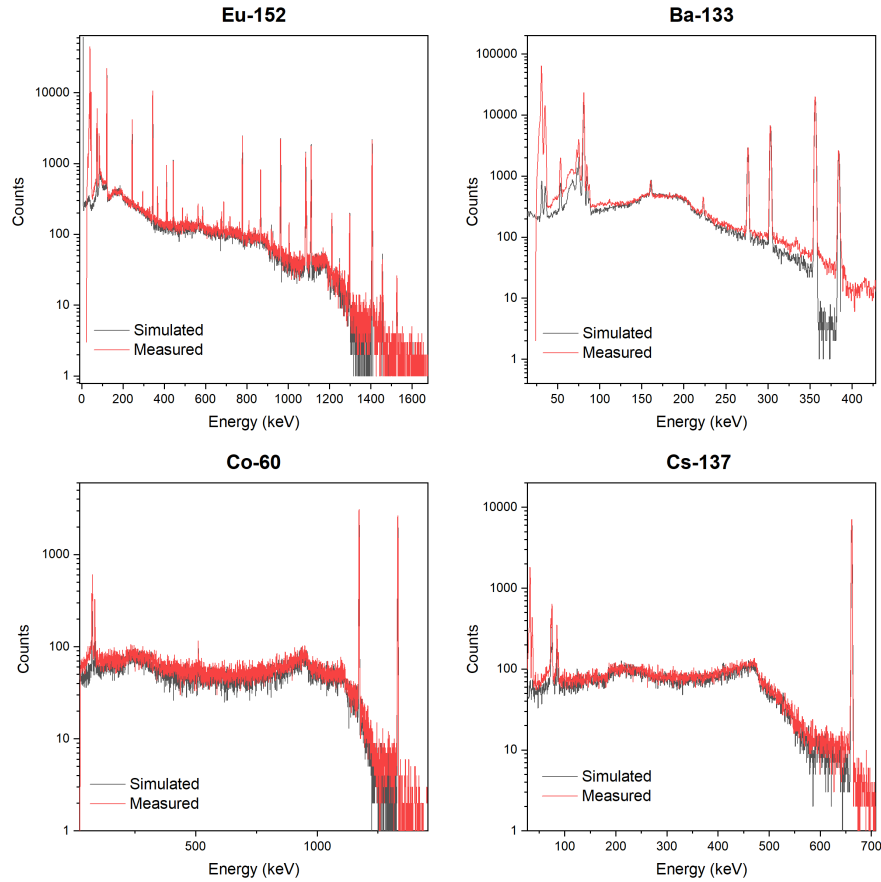


Figure 25: Comparison between measured and MCNP6 simulated γ -ray spectra for ^{137}Cs , ^{60}Co , ^{133}Ba , and ^{152}Eu for ADC2.

efficiencies calculated for the γ -ray energy match with the energy efficiency model (described in Section 3.3.4). The red points are the calculated efficiencies using the net peak area from the simulated spectra and the emissions from the source. While most of these points are within $\pm\sigma$ of the model, the efficiency of the simulated 122 keV γ -ray is significantly less. Despite being within $\pm 5\%$ difference from the net peak area, there are a few that deviate slightly from the model. The net peak area of individual γ -rays is directly used to calculate the fission product yields, so

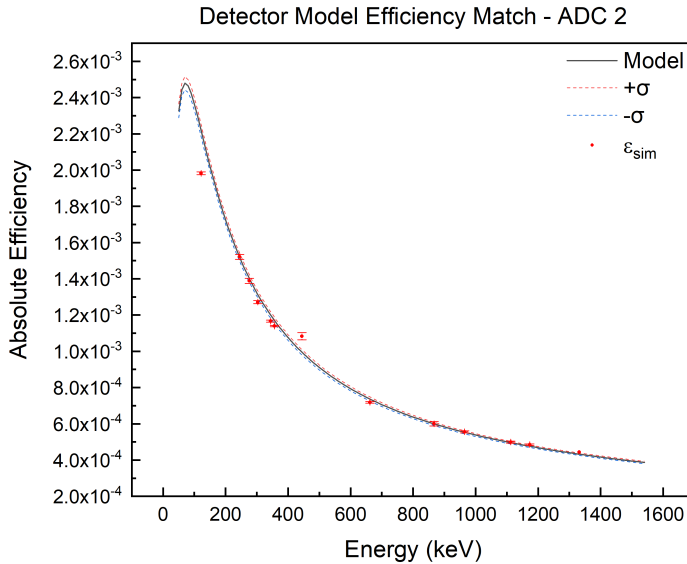


Figure 26: Match of the energy efficiency of simulated γ -ray spectra to experimentally produced efficiency model.

keeping that value within 5% has more weight than matching the efficiency model exactly.

The shape of the simulated and measured γ -ray spectra does not exactly match at low energies (seen especially with the ^{133}Ba in Figure 25). To investigate this, γ -ray measurements were made with parts of the pneumatic track and surrounding shielding to ascertain whether an additional radioactive source could be contributing. At the rear exit of the polyethelene housing and lead rings, a plastic bag filled with lead shot was placed to shield against scattered photons entering the detector. This process found that the antimony impurities within the material had been activated, causing ^{124}Sb to be significantly measured within the detector. One of the β^- s emitted in the decay of ^{124}Sb is seen in the shape of the spectra that reflects a bremsstrahlung X-ray spectrum with an endpoint energy at 610 keV (I=51.7%).

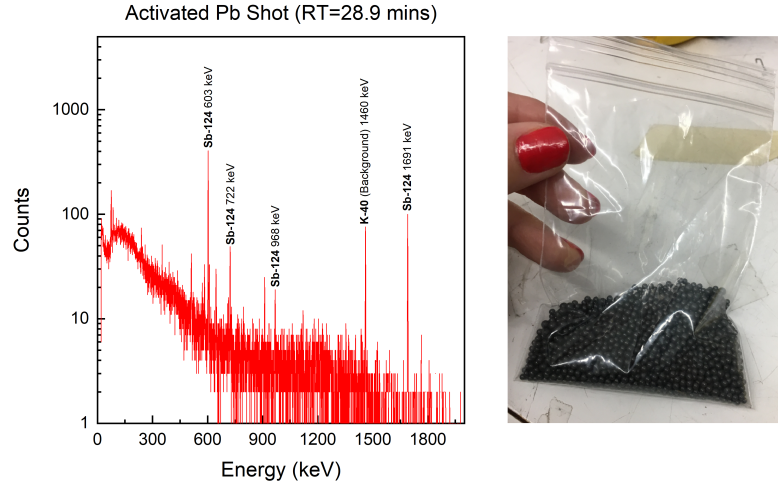


Figure 27: Measured γ -ray spectrum of the Pb shot (Left), Bagged sample of the Pb shot used as in-hall detector shielding during experiment (Right).

There were also several characteristic γ -rays which were seen in the measurement of the lead shot, such as 603 keV, 772 keV, 968 keV, and 1691 keV. Although this caused some visual discrepancy in the measured and simulated peaks, especially for ^{133}Ba , the addition of this low intensity ^{124}Sb did not significantly detract from the intended use of the HPGe response model and was not further included.

5 Results

5.1 Overview

The primary outcome of this work was the measurement of short-lived ($T_{1/2} \leq 50$ s) fission product yields with uncertainty reported. These experiments resulted in measured cumulative photofission product yields (CFPYs) for ^{238}U and ^{232}Th for the bremsstrahlung endpoint energies of 8, 14, and 20 MeV. The half-lives of the reported fission products range from 1.07-40.8 seconds, with an additional product with a 75.3 second half-life included. The excitation energy of each target nuclide is also reported in Tables 8-13.

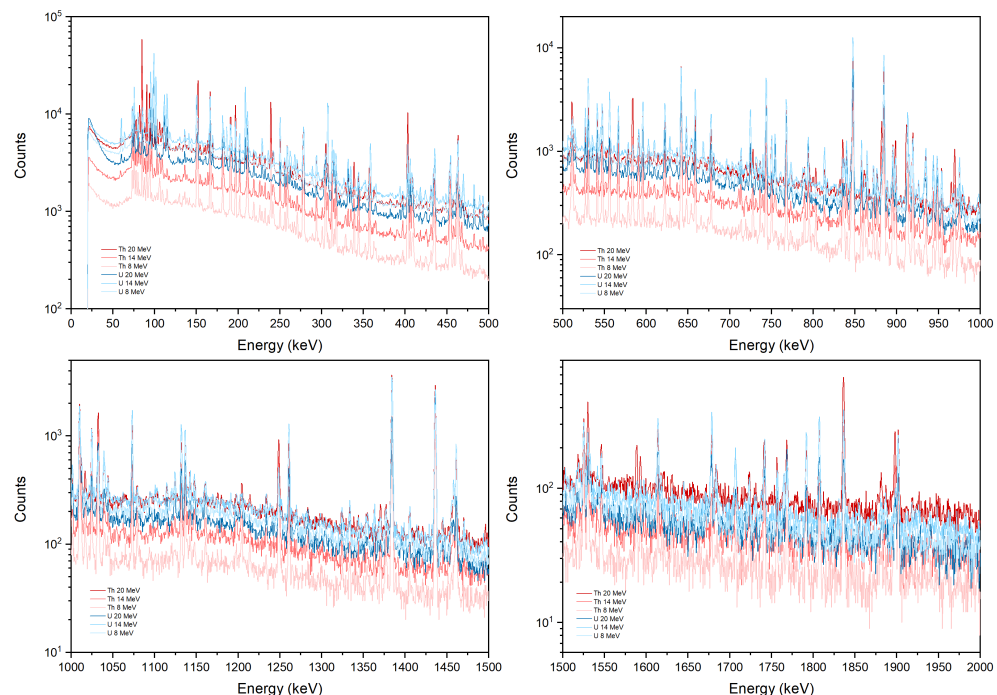


Figure 28: Summation of in-hall cycle measurements parsed from 2 to 112 s ^{232}Th and ^{238}U at $B=8$, 14, and 20 MeV from 0-500 keV (top left), 500-1000 keV (top right), 1000-1500 keV (bottom left), and 1500-2000 keV (bottom right).

Table 8: Photofission Product Yields for ^{238}U at $\langle E^*(B) \rangle = 12.59 \pm 0.01$ MeV

A	Z	Nuclide	$T_{1/2}$ (s)	β	Energy (keV)	FPY	Type
88	35	^{88}Br	16.34(8)	0.625(3)	775.28(6)	0.01149(21)	C
90	36	^{90}Kr	32.32(2)	0.390(3)	1118.69(5)	0.02337(11)	C
93	37	^{93}Rb	5.84(3)	0.202(1)	432.61(3)	0.03870(18)	C
94	37	^{94}Rb	2.702(5)	0.610(4)	836.9(1)	0.02736(13)	C
94	38	^{94}Sr	75.3(2)	0.942(9)	1427.7(1)	0.03652(17)	C
95	38	^{95}Sr	23.9(14)	0.226(12)	685.6(-)	0.04136(24)	C
96	38	^{96}Sr	1.07(1)	0.719(3)	809.4(3)	0.04045(15)	C
97	39	^{97m}Y	1.17(3)	0.921(2)	1103.3(3)	0.02054(41)	C
103	41	^{103}Nb	1.5(2)	1.00(6)	102.561(3)	0.01594(7)	C
106	43	^{106}Tc	35.6(6)	0.558(17)	270.096(9)	0.02175(10)	C
135	52	^{135}Te	19(2)	0.279(12)	603.70(3)	0.03172(15)	C
136	52	^{136}Te	17.63(9)	0.182(2)	578.75(3)	0.03610(17)	C
138	53	^{138}I	6.26(3)	0.56(3)	588.825(18)	0.02374(52)	C
139	54	^{139}Xe	39.68(14)	0.217(6)	296.53(7)	0.03989(24)	C
140	54	^{140}Xe	13.6(10)	0.20(2)	805.52(10)	0.03206(42)	C
142	55	^{142}Cs	1.684(14)	0.128(3)	1326.46(7)	0.03157(11)	C
143	56	^{143}Ba	14.5(3)	0.156(13)	798.79(2)	0.03599(30)	C
144	56	^{144}Ba	11.5(2)	0.183(4)	430.48(12)	0.02925(79)	C
144	57	^{144}La	40.8(4)	0.943(2)	397.44(9)	0.03384(16)	C

Figure 28 includes all the in-hall γ -ray spectroscopy data (total counts in a 110 s bin) produced from the in-hall cycling setup that was used in the calculation of the fission product yields. The shown γ -ray spectra are the summation of the list-mode data utilized to measure these yields for each pair of nuclide target and endpoint energy. As described in Section 3.3, during analysis the first 2 seconds following EOB of measurement data were eliminated to account for pneumatic transfer time. The in-hall detector data used in calculation of these results was limited to a maximum time of 112 seconds following EOB to account for the pneumatic transfer back to the irradiation position each cycle. This set of summed cycling measurement data was uniformly parsed into timing bins specific to the half-life and decay scheme of the nuclide of interest during analysis to maximize

Table 9: Photofission Product Yields for ^{238}U at $\langle E^*(B) \rangle = 10.30 \pm 0.01$ MeV

A	Z	Nuclide	$T_{1/2}$ (s)	β	Energy (keV)	FPY	Type
88	35	^{88}Br	16.34(8)	0.625(3)	775.28(6)	0.01762(43)	C
90	36	^{90}Kr	32.32(2)	0.390(3)	1118.69(5)	0.02536(7)	C
93	37	^{93}Rb	5.84(3)	0.202(1)	432.61(3)	0.03980(11)	C
94	37	^{94}Rb	2.702(5)	0.610(4)	836.9(1)	0.02893(7)	C
94	38	^{94}Sr	75.3(2)	0.942(9)	1427.7(1)	0.04522(12)	C
95	38	^{95}Sr	23.9(14)	0.226(12)	685.6(-)	0.05361(31)	C
96	38	^{96}Sr	1.07(1)	0.719(3)	809.40(3)	0.04499(8)	C
97	39	^{97m}Y	1.17(3)	0.921(2)	1103.3(3)	0.02226(64)	C
103	41	^{103}Nb	1.5(2)	1.00(6)	102.561(3)	0.01329(3)	C
106	43	^{106}Tc	35.6(6)	0.558(17)	270.096(9)	0.02951(8)	C
135	52	^{135}Te	19(2)	0.279(12)	603.70(3)	0.04621(13)	C
136	52	^{136}Te	17.63(9)	0.182(2)	578.75(3)	0.03350(9)	C
138	53	^{138}I	6.26(3)	0.56(3)	588.825(18)	0.03561(92)	C
139	54	^{139}Xe	39.68(14)	0.217(6)	296.53(7)	0.04667(42)	C
140	54	^{140}Xe	13.6(10)	0.20(2)	805.52(10)	0.04115(78)	C
142	55	^{142}Cs	1.684(14)	0.128(3)	1326.46(7)	0.03509(8)	C
143	56	^{143}Ba	14.5(3)	0.156(13)	798.79(2)	0.04390(30)	C
144	56	^{144}Ba	11.5(2)	0.183(4)	430.48(12)	0.03547(58)	C
144	57	^{144}La	40.8(4)	0.943(2)	397.44(9)	0.04368(20)	C

counting statistics available with this collected data.

Tables 8-13 give all of the resulting fission product data from the experiments. These list the type of fission product yield as “C” for cumulative fission product yields. The half-life ($T_{1/2}$), branching intensities (β), and γ -ray energies with associated uncertainty used in the calculations were accessed from the Evaluated Nuclear Structure Data File (ENSDF) through the National Nuclear Data Center search and retrieval system. [50]

Although the available body of published photofission product yield data is greatest for ^{238}U , little is reported for the short-lived ($T_{1/2} \leq 50$ s) fission products measured in this work. The published data for short-lived ^{238}U by Clercq *et al.* [23] includes several of the same fission products, but is reported in the form

Table 10: Photofission Product Yields for ^{238}U at $\langle E^*(B) \rangle = 6.78 \pm 0.01$ MeV

A	Z	Nuclide	$T_{1/2}$ (s)	β	Energy (keV)	FPY	Type
88	35	^{88}Br	16.34(8)	0.625(3)	775.28(6)	0.02193(25)	C
90	36	^{90}Kr	32.32(2)	0.390(3)	1118.69(5)	0.04817(12)	C
93	37	^{93}Rb	5.84(3)	0.202(1)	432.61(3)	0.04679(11)	C
94	37	^{94}Rb	2.702(5)	0.610(4)	836.9(1)	0.03802(9)	C
94	38	^{94}Sr	75.3(2)	0.942(9)	1427.7(1)	0.05983(18)	C
95	38	^{95}Sr	23.9(14)	0.226(12)	685.6(-)	0.06717(40)	C
96	38	^{96}Sr	1.07(1)	0.719(3)	809.40(3)	0.05647(73)	C
97	39	^{97m}Y	1.17(3)	0.921(2)	1103.3(3)	0.05840(14)	C
103	41	^{103}Nb	1.5(2)	1.00(6)	102.561(3)	0.04790(3)	C
106	43	^{106}Tc	35.6(6)	0.558(17)	270.096(9)	0.03904(10)	C
135	52	^{135}Te	19(2)	0.279(12)	603.70(3)	0.06645(17)	C
136	52	^{136}Te	17.63(9)	0.182(2)	578.75(3)	0.04236(7)	C
138	53	^{138}I	6.26(3)	0.56(3)	588.825(18)	0.06232(48)	C
139	54	^{139}Xe	39.68(14)	0.217(6)	296.53(7)	0.06956(44)	C
140	54	^{140}Xe	13.6(10)	0.20(2)	805.52(10)	0.06835(99)	C
142	55	^{142}Cs	1.684(14)	0.128(3)	1326.46(7)	0.04304(5)	C
143	56	^{143}Ba	14.5(3)	0.156(13)	798.79(2)	0.05550(123)	C
144	56	^{144}Ba	11.5(2)	0.183(4)	430.48(12)	0.04304(5)	C
144	57	^{144}La	40.8(4)	0.943(2)	397.44(9)	0.06226(36)	C

of fractional cumulative chain yields. To compare with their data set, multiple fission products in the same mass chain would have needed to be measured. Wen and Yang [47] reported relative fission product yields for ^{88}Br , ^{93}Rb , ^{95}Sr , ^{106}Tc for the photofission of ^{238}U at 22 MeV endpoint energy. Due to the lack of overlapping fission products and a difference in reporting, the comparison with this work was not used. No published experimental measurements for the short-lived fission products reported in this work for ^{232}Th were available in the body of published photofission product yields.

Table 11: Photofission Product Yields for ^{232}Th at $\langle E^*(B) \rangle = 11.50 \pm 0.03$ MeV

A	Z	Nuclide	$T_{1/2}$ (s)	β	Energy (keV)	FPY	Type
88	35	^{88}Br	16.34(8)	0.625(3)	775.28(6)	0.03236(23)	C
90	36	^{90}Kr	32.32(2)	0.390(3)	1118.69(5)	0.04936(28)	C
93	37	^{93}Rb	5.84(3)	0.202(1)	432.61(3)	0.03894(15)	C
94	37	^{94}Rb	2.702(5)	0.610(4)	836.9(1)	0.02028(7)	C
94	38	^{94}Sr	75.3(2)	0.942(9)	1427.7(1)	0.03705(17)	C
95	38	^{95}Sr	23.9(14)	0.226(12)	685.6(-)	0.04683(42)	C
96	38	^{96}Sr	1.07(1)	0.719(3)	809.40(3)	0.01778(81)	C
106	43	^{106}Tc	35.6(6)	0.558(17)	270.096(9)	0.01126(15)	C
135	52	^{135}Te	19(2)	0.279(12)	603.70(3)	0.03836(15)	C
136	52	^{136}Te	17.63(9)	0.182(2)	578.75(3)	0.02513(75)	C
138	53	^{138}I	6.26(3)	0.56(3)	588.825(18)	0.02074(20)	C
139	54	^{139}Xe	39.68(14)	0.217(6)	296.53(7)	0.05088(94)	C
140	54	^{140}Xe	13.6(10)	0.20(2)	805.52(10)	0.02467(75)	C
143	56	^{143}Ba	14.5(3)	0.156(13)	798.79(2)	0.03054(43)	C
144	56	^{144}Ba	11.5(2)	0.183(4)	430.48(12)	0.03785(104)	C
144	57	^{144}La	40.8(4)	0.943(2)	397.44(9)	0.03682(27)	C

5.2 Fission Product Yields for ^{238}U

The calculated CFPYs for each ^{238}U experiment are given in Tables 8-10. Table 8 lists the 19 measured CFPYs for endpoint energy of 20 MeV or excitation energy, $\langle E^*(B) \rangle$, of 12.59 ± 0.01 MeV. Table 9 lists the 19 measured CFPYs for endpoint energy of 14 MeV or excitation energy, $\langle E^*(B) \rangle$, of 10.30 ± 0.01 MeV. Table 10 lists the 19 measured CFPYs for endpoint energy of 8 MeV or excitation energy, $\langle E^*(B) \rangle$, of 6.78 ± 0.01 MeV. The same fission products are reported for all three energies.

For the three endpoint energies, 8 cumulative fission product yields were measured on the low mass peak of the fission product yield curve ($A=88-106$). Two of these CFPYs, ^{94}Rb and ^{94}Sr , can be used to calculate the independent fission product yield of ^{94}Rb for each excitation energy. On the high mass peak of the

Table 12: Photofission Product Yields for ^{232}Th at $\langle E^*(B) \rangle = 9.22 \pm 0.01$ MeV

A	Z	Nuclide	$T_{1/2}$ (s)	β	Energy (keV)	FPY	Type
88	35	^{88}Br	16.34(8)	0.625(3)	775.28(6)	0.04337(28)	C
90	36	^{90}Kr	32.32(2)	0.390(3)	1118.69(5)	0.06570(35)	C
93	37	^{93}Rb	5.84(3)	0.202(1)	432.61(3)	0.04925(15)	C
94	37	^{94}Rb	2.702(5)	0.610(4)	836.9(1)	0.02067(6)	C
94	38	^{94}Sr	75.3(2)	0.942(9)	1427.7(1)	0.04622(19)	C
95	38	^{95}Sr	23.9(14)	0.226(12)	685.6(-)	0.05698(43)	C
96	38	^{96}Sr	1.07(1)	0.719(3)	809.40(3)	0.01128(46)	C
136	52	^{136}Te	17.63(9)	0.182(2)	578.75(3)	0.02332(39)	C
138	53	^{138}I	6.26(3)	0.56(3)	588.825(18)	0.02810(24)	C
139	54	^{139}Xe	39.68(14)	0.217(6)	296.53(7)	0.07762(81)	C
140	54	^{140}Xe	13.6(10)	0.20(2)	805.52(10)	0.04399(119)	C
143	56	^{143}Ba	14.5(3)	0.156(13)	798.79(2)	0.03704(76)	C
144	56	^{144}Ba	11.5(2)	0.183(4)	430.48(12)	0.05370(52)	C
144	57	^{144}La	40.8(4)	0.943(2)	397.44(9)	0.07199(41)	C

fission product yield curve ($A=135\text{-}144$), eleven CFPYs were measured.

Of the ^{238}U fission products measured, ^{90}Kr , ^{144}La , and ^{139}Xe were indicated as short-lived fission products of note as signatures in the photofission of ^{238}U in 9 MeV X-ray induced active interrogation by Wehe *et al.* [39] These photofission products were identified in their work, but the cumulative fission product yields were not reported. The fission products from ^{238}U photofission indicated by Wehe *et al.* [39] with half-lives of less than 50 s were considered initially as fission product yields of interest to acquire. The cumulative fission product yields ^{90}Kr , ^{144}La , and ^{139}Xe for ^{238}U are listed in Tables 8-10.

The measured cumulative fission product yields for ^{97m}Y were compared against the ENDF-B/VII.0 cumulative fission product yields for $^{238}\text{U}(n, f)$ at incident neutron energies of 500 keV and 14 MeV. ENDF-B/VII.0 listed both these CFPYs for ^{97m}Y as zero, but ^{97m}Y was measured in our experiments at a yield of $2.054\% \pm 0.041\%$ for 20 MeV, $2.23\% \pm 0.64\%$ for 14 MeV and $5.84\% \pm 0.14\%$ for 8

Table 13: Photofission Product Yields for ^{232}Th at $\langle E^*(B) \rangle = 6.74 \pm 0.02$ MeV

A	Z	Nuclide	$T_{1/2}$ (s)	β	Energy (keV)	FPY	Type
88	35	^{88}Br	16.34(8)	0.625(3)	775.28(6)	0.06395(44)	C
90	36	^{90}Kr	32.32(2)	0.390(3)	1118.69(5)	0.08660(47)	C
93	37	^{93}Rb	5.84(3)	0.202(1)	432.61(3)	0.05225(13)	C
94	37	^{94}Rb	2.702(5)	0.610(4)	836.9(1)	0.02579(9)	C
94	38	^{94}Sr	75.3(2)	0.942(9)	1427.7(1)	0.05344(25)	C
95	38	^{95}Sr	23.9(14)	0.226(12)	685.6(-)	0.07190(49)	C
96	38	^{96}Sr	1.07(1)	0.719(3)	809.40(3)	0.02163(73)	C
135	52	^{135}Te	19(2)	0.279(12)	603.70(3)	0.04288(11)	C
136	52	^{136}Te	17.63(9)	0.182(2)	578.75(3)	0.01948(62)	C
138	53	^{138}I	6.26(3)	0.56(3)	588.825(18)	0.03552(40)	C
139	54	^{139}Xe	39.68(14)	0.217(6)	296.53(7)	0.08452(58)	C
140	54	^{140}Xe	13.6(10)	0.20(2)	805.52(10)	0.05993(140)	C
143	56	^{143}Ba	14.5(3)	0.156(13)	798.79(2)	0.08972(91)	C
144	56	^{144}Ba	11.5(2)	0.183(4)	430.48(12)	0.09596(86)	C
144	57	^{144}La	40.8(4)	0.943(2)	397.44(9)	0.10232(59)	C

MeV. The $B=20$ MeV CFPY compared well with the CFPY for ^{97m}Y (1103 keV) reported for 14 MeV neutron fission by Pierson *et al.* [37] of $2.011\% \pm 0.170\%$.

The CFPYs for ^{103}Nb ($T_{1/2}=1.5$ s) were difficult to measure due to low intensity of the 102.6 keV γ -ray peak and interference with the peaks nearest to 102.6 keV. Measurement of the CFPY daughter product, ^{103}Mo ($T_{1/2}=67.5$ s), was attempted as a way to gauge the scale of the independent yield of ^{103}Nb . The delayed γ -rays of ^{103}Mo were not seen in high enough intensity to be used to calculate the CFPY, despite a relatively high reported CFPY in ENDF-B/VII.0 for 500 keV ($6.27\% \pm 0.38\%$) and 14 MeV ($4.60\% \pm 0.37\%$) neutron fission for ^{103}Mo . The CFPYs of ^{103}Nb that are reported in Tables 8-10 are intended primarily as an indication that the CFPY reported in ENDF-B/VII.0 for neutron fission may be considerably higher than was measured for photofission of ^{238}U .

No short-lived CFPY were could be measured for the “valley” of the fission

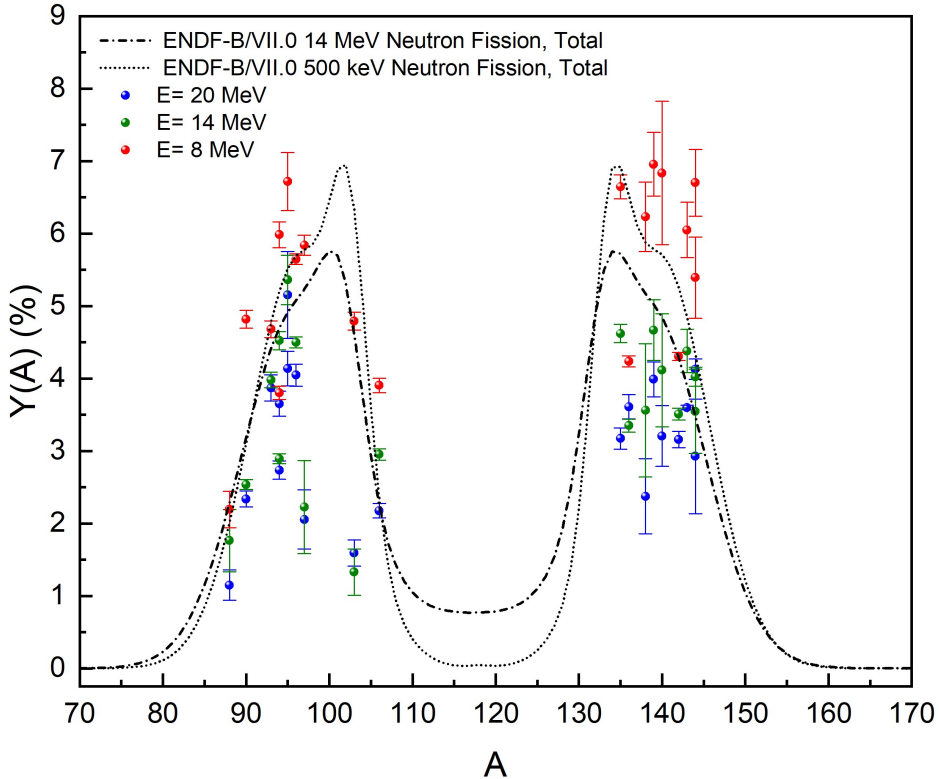


Figure 29: Short-lived CFPY of ^{238}U at all three energies with respect to the multimode-fission model fit to ENDF-B/VII.0 fast and DT neutron fission fractional mass yields.

product yield curve for ^{238}U at any energy. Despite not being able to measure valley isotopes due to their low intensity, it may be possible to determine useful ratios of CFPY for use in nuclear forensics analysis using products on the sides of the high or low mass peaks. These FPY may be used to give indication of incident energy based on relative shape of the STI and STII modes change with respect to excitation energy.

Figure 29 is a graphical representation of the reported photofission CFPYs of ^{238}U . Figure 31 reports the CFPYs for the endpoint energies of 8 MeV (bottom), 14 MeV (middle), and 20 MeV (top). The sum of the SL, STI, and STII fission modes was fit to fractional mass yield data from ENDF-B/VII.0 for both the fast

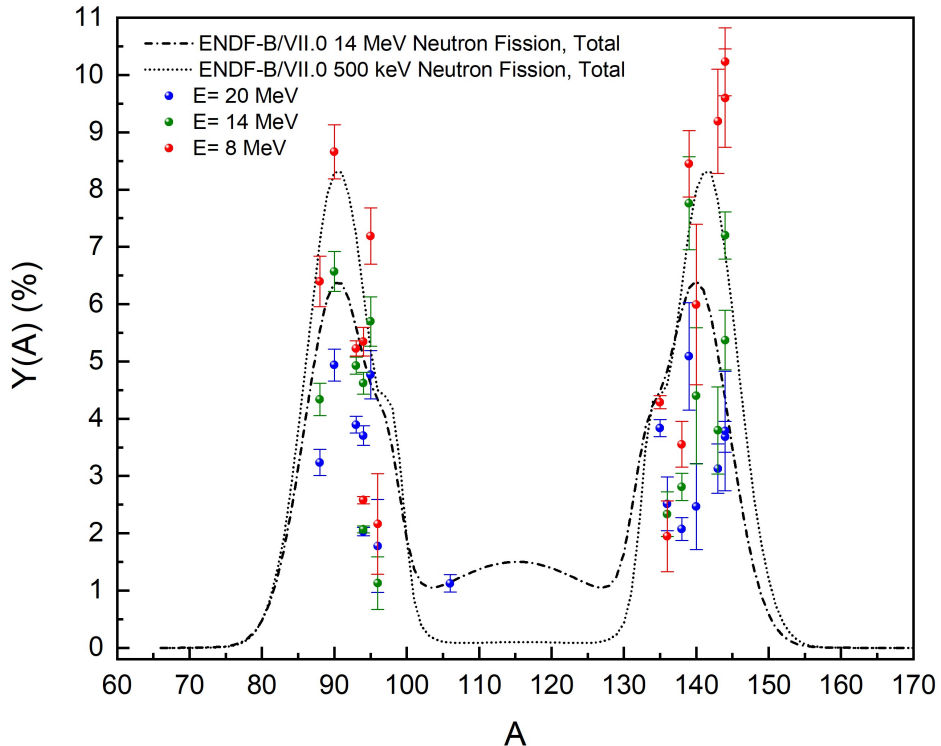


Figure 30: Short-lived CFPY of ^{232}Th at all three energies with respect to the multimode-fission model fit to ENDF-B/VII.0 fast and DT neutron fission fractional mass yields.

and DT neutron fission of ^{238}U and are included as a reference to expected values. In this way, the relative difference in the CFPY with respect to energy and the varying intensity in the fission modes between 500 keV and 14 MeV neutron can more clearly be seen. Thermal fission was not used as a reference as ^{238}U and ^{232}Th are both fissionable nuclides with a threshold energy for neutron fission that requires energies higher than thermal neutrons.

5.3 Fission Product Yields for ^{232}Th

The calculated cumulative fission product yields for each ^{232}Th experiment are given in Tables 11-13. Table 11 lists the 16 measured cumulative fission product

yields for an endpoint energy of 20 MeV or excitation energy of 11.50 ± 0.03 MeV. Table 12 lists the 14 measured cumulative fission product yields for an endpoint energy of 14 MeV or excitation energy of 9.22 ± 0.01 MeV. Table 13 lists the 15 measured cumulative fission product yields for an endpoint energy of 8 MeV or excitation energy of 6.74 ± 0.02 MeV. Compared to the ^{238}U measurements, the statistics of the ^{232}Th counts were not as good due to a lower cross section. In the $B=14$ and $B=8$ MeV experiments of ^{232}Th , 10 additional cycles were added to achieve better counting statistics.

The cumulative fission product yields for ^{97m}Y were attempted for the three ^{232}Th excitation energies. The CFPY for ^{97m}Y (1103 keV) reported by Pierson *et al.* [37] in their measurements of short-lived products of 14 MeV neutron fission of ^{232}Th was $0.81\% \pm 0.12\%$ and suggests the intensity of the 1103.0 keV γ -ray is potentially too low in the ^{232}Th data to extract the CFPYs.

Only in the 20 MeV irradiation for ^{232}Th was it possible to confidently calculate the ^{106}Tc cumulative fission product yield. Although it was on the low mass peak for the ^{238}U data, ^{106}Tc is in the valley of the ^{232}Th fission product curve. Measurement of ^{106}Tc was in agreement with the expectation of the “third peak” seen in the high-energy fission of ^{232}Th due to the increased dependence on the symmetric mode. Ideally, more fission product yields in the valley of the fission product yield curve would be measured, but due to their relatively low yield and the difficulty of measuring such short-lived fission products, using longer-lived fission product yield data to compare the peak-to-valley ratio for each of the photofission product yield curves may be more achievable.

Figure 30 is a graphical representation of the reported photofission CFPYs of ^{232}Th for each energy. Figure 32 reports the CFPYs for the endpoint energies of 8

MeV (bottom), 14 MeV (middle), and 20 MeV (top). The sum of the SL, STI, and STII fission modes was fit to fractional mass yield data from ENDF-B/VII.0 for both the fast and DT neutron fission of ^{232}Th as a reference (previously discussed in Section 2.1.2). These were used rather than neutron-induced fission of ^{237}U and ^{231}Th due to superior experimental fission product yield data. Additionally, matching the fission product yield distribution to ^{238}U and ^{232}Th neutron fission is more useful in isotope production for nuclear forensic exercises. There is good agreement between the 20 MeV CFPY data and the DT neutron fission of ^{232}Th , especially seen in the inclusion of the ^{106}Tc CFPY. The photofission CFPYs of each energy appear to also reflect the general shape of the asymmetric modes that shape the high and low mass peaks.

An important consideration in this comparison is that the short-lived fission products are at the start of their respective mass chains and are being compared with the fractional mass yields from ENDF-B/VII.0, so they are expected be less than the total fraction mass yield for the complete mass chain.

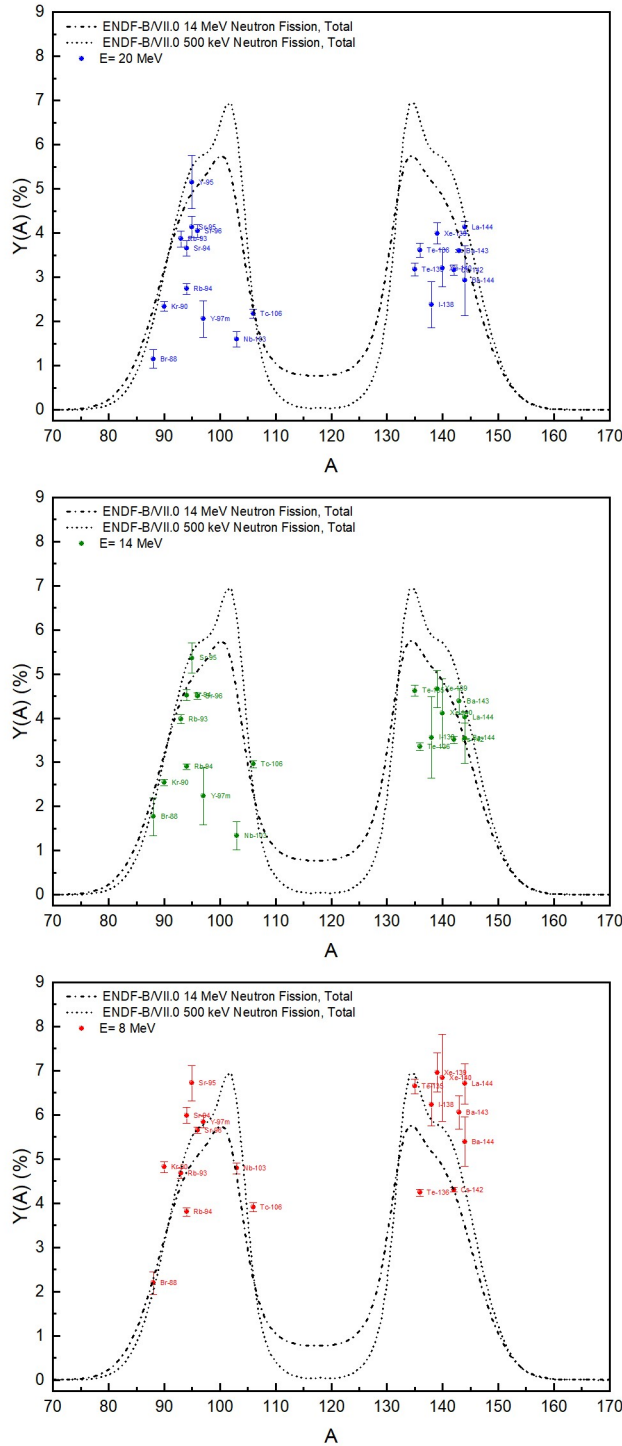


Figure 31: Short-lived CFPY of ^{238}U at endpoint energies 20 MeV (top), 14 MeV (middle), and 8 MeV (bottom) with respect to the multimode-fission model fit to ENDF-B/VII.0 fast and DT neutron fission fractional mass yields.

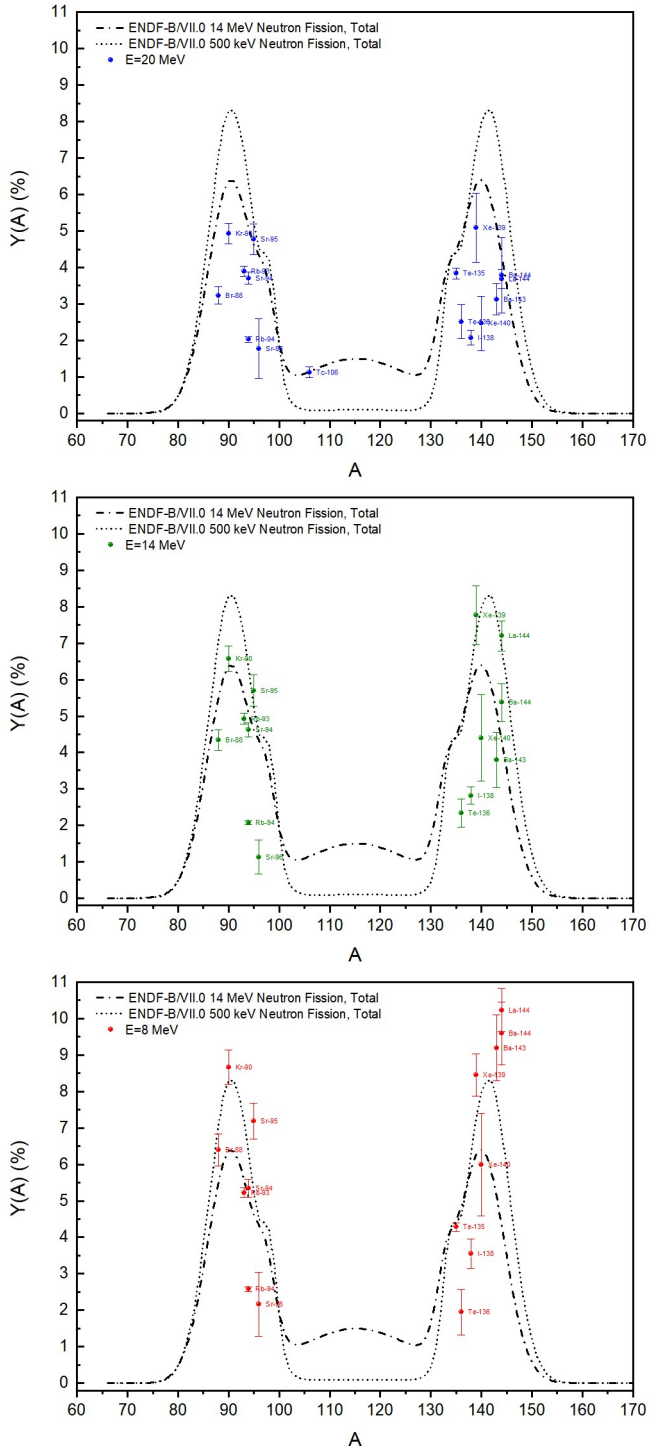


Figure 32: Short-lived CFPY of ^{232}Th at endpoint energies 20 MeV (top), 14 MeV (middle), and 8 MeV (bottom) with respect to the multimode-fission model fit to ENDF-B/VII.0 fast and DT neutron fission fractional mass yields.

6 Conclusions

Short-lived fission product yields were experimentally measured for ^{238}U and ^{232}Th at three bremsstrahlung X-ray endpoint energies: 8, 14, and 20 MeV. These are reported with both the endpoint energy and the target excitation energy to allow for better comparison among the body of published photofission work. Due to the lack of evaluated experimental data for photofission product yields, ENDF-B/VII.0 neutron fission cumulative fission product yields for fast (500 keV) and DT (14 MeV) neutron fission were used as the primary comparison to the measured photofission yields. Overall, the photofission CFPYs for ^{238}U and ^{232}Th at endpoint energy of 20 MeV were in good agreement with the ENDF-B/VII.0 DT neutron fission, while the 14 and 8 MeV CFPYs for both targets appear to reflect the expected distribution of the multimode-fission model using the ENDF-B/VII.0 fractional mass yields.

The reported absolute uncertainty of the photofission product yields was calculated with all factors considered where data were available or acquired through simulation. A thorough characterization of the detector and experimental setup aided in the confidence of the measurements and report of low uncertainty on many of the CFPYs. Extensive simulations were performed to verify the neutron fission and impurity actinide fissions were negligible for both targets. ENDF-B/VII.0 lacks reported uncertainty on the photonuclear cross sections used in this work, which, if available, would likely be a significant contributor to the total uncertainty of the experimentally measured fission product yields.

6.1 Future Work

These short-lived fission product yields of ^{238}U and ^{232}Th will be combined with a set of relatively longer-lived ($T_{1/2} > 50$ s) photofission product yields from the same irradiated targets, using post-irradiation auxiliary counting lab measurements. The combination of these two data sets allows for a larger amount of independent fission product yields to be calculated where multiple nuclides in a mass chain are measured, as well as analysis of the charge distribution of the fission products. With the inclusion of longer-lived fission product yields, the multimode-fission model will be applied to the combined set of experimental measurements. Multimode-fission model fitting was not possible with only the short-lived products in this work due to a lack of valley products and others in each mass chain.

A majority of the current photofission product yields that study the relationship between the multimode-fission modes and the target excitation energy focuses on bremsstrahlung endpoint energies higher than 20 MeV, but the lower excitation energies in this work are most useful for nuclear forensics applications and the interest in surrogate neutron fission material. There are few published photofission product yields for low (≤ 12 MeV) excitation energy photofission product yields, so future work looking at photofission excitation energies with comparable excitation energies of thermal, fast, and DT neutron fission would be of considerable value. Photofission product yield data for relatively low energy is also of utility in cargo scanning applications and other photon-induced active interrogation methods, such as in [39].

This work developed and tested the experimental and analysis methods to allow for consistent future short-lived photofission product yield calculations. Although ^{238}U and ^{232}Th have the most published experimental data, data on fission prod-

uct yields of fissile nuclides would be quite useful for forensics application. Future targets such as ^{239}Pu and ^{252}Cf are of interest, but their analysis will require consideration of thermal neutron fission and spontaneous fission.

BIBLIOGRAPHY

- [1] C. Bowman, E. Arthur, P. Lisowski, and G. Lawrence, “Nuclear energy generation and waste transmutation using an accelerator-driven intense thermal neutron source,” *Nuclear Instruments and Methods in Physics Research Section A*, vol. 320, pp. 336–367, 2002.
- [2] S. Leray, F. Borne, S. Crespin, J. Frehaut, X. Ledoux, E. Martinez, Y. Patin, E. Petibon, P. Pras, A. Boudard, R. Legrain, Y. Terrien, F. Brochard, and D. Drake, “Spallation neutron production by 0.8, 1.2, and 1.6 gev protons on various targets,” *Physical Review C*, vol. 65, 2002.
- [3] S. Degweker, P. Bhagwat, S. Krishnagopal, and A. Sinha, “Physics and technology for development of accelerator driven systems in india,” *Progress in Nuclear Energy*, vol. 101, no. A, pp. 53–81, 2017.
- [4] T. Gozani, “Active nondestructive assay of nuclear materials,” tech. rep., Report NUREG/CR-0602, United States Regulatory Commission, 1981.
- [5] G. Baldwin and G. Klaiber, “Photo-fission in heavy elements,” *Physical Review*, vol. 71, pp. 3–10, Jan. 1947.
- [6] B. L. Berman and S. Fultz, “Measurements of the giant dipole resonance with monoenergetic photons,” *Reviews of Modern Physics*, vol. 47, pp. 713–761, July 1975.
- [7] M. T. Kinlaw, “A study of fission modes to improve nuclear forensics,” *Idaho National Laboratory, INL/MS-17-40860*, 2017.
- [8] K. J. Moody, I. D. Hutcheon, and P. M. Grant, *Nuclear Forensic Analysis*. Taylor & Francis Group, 2005.
- [9] “Nuclear forensics: Role, state of the art, and program needs,” tech. rep., Joint Working Group of the American Physical Society and the American Association for the Advancement of Science, June 2013.
- [10] C. Wagemans, *The Nuclear Fission Process*. CRC Press, London, 1990.
- [11] K. K. Shultz and R. E. Faw, *Fundamentals of Nuclear Science and Engineering*. CRC Press, 2nd ed., 2008.
- [12] “Handbook on photonuclear data for applications, cross-sections and spectra,” Tech. Rep. IAEA-TECDOC-1178, International Atomic Energy Agency, Oct. 2000.

- [13] Y. P. Gangrsky, S. Zemlyanoi, D. Karaivanov, K. Marinova, B. Markov, L. Menikova, G. Mishinsky, Y. E. Penionzhkevich, and V. Zhemenik, “Production of photofission fragments and study of their nuclear structure by laser spectroscopy,” *Letters on Nuclei (trans.)*, vol. 2, no. 2, pp. 50–59, 2005.
- [14] S. Belyshev, B. Ishkhanov, A. Kuznetsov, and K. Stopani, “Mass yield distributions and fission modes in photofission of ^{238}U below 20 mev,” *Physical Review C*, vol. 91, 2015.
- [15] J. M. Verbeke, C. Hangmann, and D. Wright, “Simulation of neutron and gamma ray emission from fission and photofission,” Tech. Rep. UCRL0AR-228518, Lawrence Livermore National Laboratory, May 2010.
- [16] C. Segebade, H.-P. Weise, and G. Lutz, *Photon Activation Analysis*, vol. 1. De Gruyter, 1987.
- [17] T. Shizuma, “Photonuclear reaction data measurements and interpretation, japan atomic energy agency.” PDF.
- [18] B. Ishkhanov and A. Kuznetsov, “ ^{238}U photofission in the energy region of the giant dipole resonance,” *Physics of Atomic Nuclei*, vol. 77, no. 7, pp. 824–833, 2014.
- [19] N. Demekhina and G. Karapetyan, “Symmetric and asymmetric modes of ^{232}Th photofission at intermediate energies,” *Physics of Atomic Nuclei*, vol. 73, no. 1, pp. 24–33, 2010.
- [20] B. Ishkhanov and A. Kuznetsov, “The mass distributuon of ^{238}U photofission fragments,” *Moscow University Physics Bulletin*, vol. 68, no. 4, pp. 279–287, 2013.
- [21] M. Pahlavani and P. Mehdipour, “Study of the photofission fragment mass distribution of ^{232}Th , ^{238}U , ^{237}Np , and ^{240}Pu isotopes in various γ -ray energies,” *International Journal of Modern Physics E*, vol. 27, no. 3, pp. 1–13, 2018.
- [22] H. Niak, F. Carrel, G. Kim, A. Sari, S. Normand, and A. Goswami, “Mass yield distributions of fission products from photo-fission of ^{238}U ,” *The European Physical Journal A*, vol. 49, no. 94, pp. 1–23, 2013.
- [23] A. D. Clercq, H. Thierens, D. D. Frenne, P. D. Gelder, P. D’Hondt, E. Jacobs, and A. Deruytter, “Method for the determination of the yields of short-lived fission products,” *Nuclear Instruments and Methods*, vol. 173, pp. 531–536, Feb. 1980.
- [24] Y. A. Izrael, *Radioactive Fallout after Nuclear Explosions and Accidents*, vol. 3. Elsevier Science, first ed., 2002.

- [25] J. Meason and P. Kuroda, “Photofission of ^{238}U induced by 17.5 monoenergetic gamma rays,” *Physical Review*, vol. 142, pp. 691–695, 1966.
- [26] B. Berman, M. A. Kelly, R. Bramblett, J. Caldwell, H. Davis, and S. Fultz, “Giant resonance in deformed nuclei: Photoneutron cross sections for ^{153}Eu , ^{160}Gd , ^{165}Ho , and ^{186}W ,” *Physical Review*, vol. 185, Sept. 1969.
- [27] S. Costa and C. Schaerf, eds., *Lecture Notes in Physics: Photonuclear Reactions I*. Springer-Verlag, 1977.
- [28] E. Bramanis, T. Deague, R. Hicks, R. Huges, E. Muirhead, R. Sambell, and R. Stewart, “The analysis of photonuclear yield curves,” *Nuclear Instruments and Methods*, vol. 100, pp. 59–71, 1972.
- [29] G. F. Knoll, *Radiation Detection and Measurement*. John Wiley & Sons, 4th ed., 2010.
- [30] J. Chadwick and M. Goldhaber, “A ‘nuclear photo-effect’: Disintegration of the dipolon by γ -rays,” *Nature*, vol. 134, pp. 237–238, Aug. 1934.
- [31] N. Tsoulfandis and S. Landsberger, *Measurement and Detection of Radiation*. CRC Press, 3rd ed., 2011.
- [32] X. Wen, J. Kavouras, D. R. Nakazawa, and H. Yang, “Simulation and measurement of delayed γ -rays after photon-induced fission,” *Nucl. Instrum. Methods Phys. Res. A*, vol. 729, pp. 781–787, 2013.
- [33] P. Sibczynski, J. Kownacki, A. Syntfeld-Kazuch, M. Moszynski, M. Kisielinski, W. Czarnacki, K. Kosinski, M. Matusiak, M. Klimasz, M. Kowalczyk, T. Abraham, J. Mierzejewski, and J. Srebrny, “Decay chains and photofission investigation based on nuclear spectroscopy of highly enriched uranium sample,” *Applied Radiation and Isotopes*, vol. 82, pp. 170–174, 2013.
- [34] H. Yang, D. Wehe, and D. Bartels, “Spectroscopy of high rate events during active interrogation,” *Nucl. Instr and Meth. in Phys. Res. A.*, vol. 598, pp. 779–787, 2009.
- [35] X. Wen, D. Nakazawa, M. Kastner, and J. Pavlick, “Evaluation of a modified hpge preamplifier for high-rate spectroscopy measurements in a pulsed photonuclear environment,” *Nuclear Technology*, vol. 784, pp. 269–273, 2016.
- [36] E. T. E. Reedy, “Discrete γ -rays from photofission for nuclear forensics applications,” Master’s thesis, Idaho State University, Dec. 2011.
- [37] B. Pierson, L. Greenwood, M. Flaska, and S. Pozzi, “Fission product yields from ^{232}Th , ^{238}U , and ^{235}U using 14 mev neutrons,” *Nuclear Data Sheets*, vol. 139, pp. 171–189, 2017.

- [38] B. Ishkhanov and S. Y. Troschiev, “Simulation of gamma-activation experiments,” *Moscow University Physics Bulletin*, vol. 68, no. 2, pp. 110–113, 2013.
- [39] D. Wehe, H. Yang, and M. Jones, “Observation of ^{238}U photofission products,” *IEEE Transactions on Nuclear Science*, vol. 53, June 2006.
- [40] D. Swindle, R. Wright, K. Takahashi, W. Rivera, and J. Meason, “Mass distribution of fission products following photofission of uranium-238,” *Nuclear Science and Engineering*, vol. 52, no. 4, pp. 466–473, 1973.
- [41] D. Bhowmick, D. Atta, D. Basu, and A. Chakrabarti, “Yields of neutron-rich nuclei by actinide photofission in giant dipole resonance region,” *Physics Review C*, vol. 91, 2015.
- [42] J. Smith and A. Richardson, “Independent yields from the photofission of ^{232}Th , and the Z_1 and statistical-dynamic models,” *Physical Review C*, vol. 44, pp. 1118–1127, Sept. 1991.
- [43] M. Berger, J. Hubbell, S. Seltzer, J. Chang, J. Coursey, R. Sukumar, D. Zucker, and K. Olsen, “Xcom: Photon cross section database (version 1.5).” <http://physics.nist.gov/xcom>, 2010.
- [44] J. Coursey, D. Schwab, J. Tsai, and R. Dragoset, “Atomic weights and isotopic compositions with relative atomic masses (version 4.1),” *National Institute of Standards*.
- [45] J. Rosenblatt, *Particle Acceleration*. Methuen & Co. LTD, 1968.
- [46] “Facilities.” Online. Idaho State University Idaho Accelerator Center, <http://iac.isu.edu/facilities.html>.
- [47] X. Wen and H. Yang, “Study on pulse processing algorithm based on template-matching for high-throughput spectroscopy,” *Nucl. Instr. and Meth. in Phys. Res. A*, vol. 784, 2015.
- [48] L. Geraldo and D. Smith, “Covariance analysis and fitting of germanium gamma-ray detector efficiency calibration data,” *Nuclear Instruments and Methods in Physics Research Section A: Accelerators, Spectrometers, Detectors and Associated Equipment*, vol. 290, no. 2, pp. 499–508, 1990.
- [49] Y. S. Sheela, H. Niak, M. M. Prasad, S. Ganesan, N. S. Nair, and S. Suryanarayana, “Covariance analysis of efficiency calibration of hpge detector,” Tech. Rep. MU/STATISTICS/DAE-BRNS/2017/1, Department of Statistics, Manipal University, Manipal, Karnataka, India, Feb. 2017.
- [50] “Evaluated nuclear structure data file search and retrieval.” National Nuclear Data Center, Brookhaven National Laboratory, <https://www.nndc.bnl.gov/ensdf/>.